




## Article

# [Tc(NO)Cl<sub>2</sub>(PPh<sub>3</sub>)<sub>2</sub>(CH<sub>3</sub>CN)] and Its Reactions with 2,2'-Dipyridyl Dichalcogenides

 Till Erik Sawallisch <sup>1</sup> , Susanne Margot Rupf <sup>1</sup> , Abdullah Abdulkader <sup>1</sup>, Moritz Johannes Ernst <sup>1</sup>, Maximilian Roca Jungfer <sup>2,\*</sup> and Ulrich Abram <sup>1,\*</sup> 
<sup>1</sup> Institute of Chemistry and Biochemistry, Freie Universität Berlin, Fabeckstr. 34/36, 14195 Berlin, Germany; t.sawallisch@hzdr.de (T.E.S.); susianne95@zedat.fu-berlin.de (S.M.R.); abdullah.abdulkader@yahoo.com (A.A.); ernstm96@zedat.fu-berlin.de (M.J.E.)

<sup>2</sup> Institute of Organic Chemistry, Ruprecht-Karls Universität Heidelberg, Im Neuenheimer Feld 270, 69120 Heidelberg, Germany

\* Correspondence: m.roca.jungfer@gmail.com (M.R.J.); ulrich.abram@fu-berlin.de (U.A.)

**Abstract:** The sparingly soluble technetium(I) complex [Tc<sup>I</sup>(NO)Cl<sub>2</sub>(PPh<sub>3</sub>)<sub>2</sub>(CH<sub>3</sub>CN)] (**1**) slowly dissolves during reactions with 2,2'-dipyridyl ditelluride, (2-pyTe)<sub>2</sub>, 2,2'-dipyridyl diselenide, (2-pySe)<sub>2</sub>, or 2,2'-dipyridyl disulfide, (2-pyS)<sub>2</sub>, under formation of deeply colored solutions. Blue (Te compound) or red solids (Se compound) of the composition [(Tc<sup>I</sup>(NO)Cl<sub>2</sub>(PPh<sub>3</sub>)<sub>2</sub>)<sub>2</sub>{μ<sub>2</sub>-(2-pyE)<sub>2</sub>}], E = Te (**3**), Se (**4**), precipitate from the reaction solutions upon addition of toluene. They represent the first technetium complexes with dichalcogenides. While [(Tc<sup>I</sup>(NO)Cl<sub>2</sub>(PPh<sub>3</sub>)<sub>2</sub>)<sub>2</sub>{μ<sub>2</sub>-(2-pyTe)<sub>2</sub>}] (**3**) is the sole product, a small amount of a second product, [Tc<sup>II</sup>(NO)Cl<sub>2</sub>(PPh<sub>3</sub>)<sub>2</sub>(2-pySe)] (**5**), was obtained from the respective mother solution of the reaction with the diselenide. From the corresponding reaction between **1** and (2-pyS)<sub>2</sub>, the technetium(II) compound, [Tc<sup>II</sup>(NO)Cl<sub>2</sub>(PPh<sub>3</sub>)<sub>2</sub>(2-pyS)] (**6**), could be isolated exclusively. The products were studied by single-crystal X-ray diffraction and spectroscopic methods including <sup>99</sup>Tc NMR for the technetium(I) products and EPR spectroscopy for the Tc(II) complexes. The experimental results are accompanied by DFT considerations, which help to rationalize the experimental observations.

**Keywords:** technetium; nitrosyls; dichalcogenides; 2-Pyridyl chalcogenolates; NMR; EPR; X-ray diffraction



Received: 10 January 2025

Revised: 3 February 2025

Accepted: 5 February 2025

Published: 8 February 2025

**Citation:** Sawallisch, T.E.; Rupf, S.M.; Abdulkader, A.; Ernst, M.J.; Roca Jungfer, M.; Abram, U. [Tc(NO)Cl<sub>2</sub>(PPh<sub>3</sub>)<sub>2</sub>(CH<sub>3</sub>CN)] and Its Reactions with 2,2'-Dipyridyl Dichalcogenides. *Molecules* **2025**, *30*, 793. <https://doi.org/10.3390/molecules30040793>

**Copyright:** © 2025 by the authors. Licensee MDPI, Basel, Switzerland. This article is an open access article distributed under the terms and conditions of the Creative Commons Attribution (CC BY) license (<https://creativecommons.org/licenses/by/4.0/>).

## 1. Introduction

The organic chemistry of aryl diselenides and aryl ditellurides is well-established, and, over the past years, such compounds have also found increasing interest as components of metal complexes. Several recent reviews have addressed the progress of the respective research in various fields. This includes fundamental structural chemistry but also applicational aspects of material science, biological chemistry, catalysis, or their use as components in electronic building blocks [1–9]. In addition to differently substituted phenyl chalcogenides, (ArE)<sub>2</sub>, bis(pyridyl) diselenides and ditellurides (*n*-pyE)<sub>2</sub> (Figure 1) in particular have been extensively studied [10,11]. Depending on the position of the pyridine nitrogen atom, such compounds are excellent building blocks for nanomaterials or MOFs, i.e., (4-pyE)<sub>2</sub> or (3-pyE)<sub>2</sub> [12–21], while (2-pyE)<sub>2</sub> can not only act as ligands in metal complexes but also as precursors for the synthesis of 2-pyridylchalcogenato complexes [10,11].

The pyridylchalcogenolato ligands, which can be obtained by facile reduction of the corresponding (2-pyE)<sub>2</sub> precursors, show multifaceted coordination chemistry [10,11,22–26], while molecular transition metal complexes with the parent diselenides or ditellurides are

relatively rare [27–34]. Only one compound with a ‘group 7 element’ has been reported previously, the Mn(II) complex  $[\text{Mn}\{(2\text{-pySe})_2\}\text{Br}_2]$  [27].

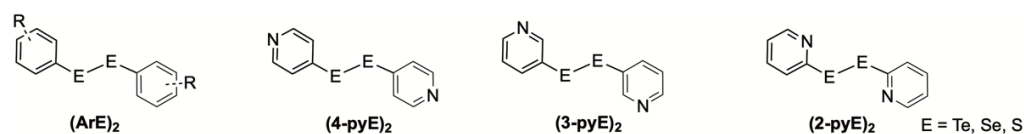


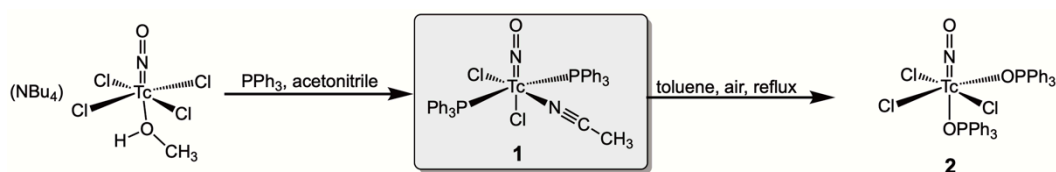
**Figure 1.** Diaryl dichalcogenides mentioned in this paper and abbreviations used.

In the present work, we report reactions of the technetium(I) nitrosyl complex  $[\text{Tc}(\text{NO})\text{Cl}_2(\text{PPh}_3)_2(\text{CH}_3\text{CN})]$  (**1**) with  $(2\text{-pyTe})_2$ ,  $(2\text{-pySe})_2$  and  $(2\text{-pyS})_2$ , describe the structures of the respective products, and compare the reactivities of the different dichalcogenides.

## 2. Results and Discussion

### 2.1. Structure and Reactivity of the Starting Complex $[\text{Tc}(\text{NO})\text{Cl}_2(\text{PPh}_3)_2(\text{CH}_3\text{CN})]$

$[\text{Tc}(\text{NO})\text{Cl}_2(\text{PPh}_3)_2(\text{CH}_3\text{CN})]$  (**1**) is readily prepared from  $(\text{NBu}_4)[\text{Tc}(\text{NO})\text{Cl}_4(\text{MeOH})]$  with  $\text{PPh}_3$  in acetonitrile (Scheme 1) [35]. An excess of triphenylphosphine acts as a reductant for the technetium(II) starting material, and the poor solubility of the product ensures a high yield and avoids the formation of side products. Although only slightly soluble, compound **1** has been successfully used as a precursor for the synthesis of a considerable number of other nitrosyltechnetium complexes [35–41]. This is most probably due to the reported gradual decomposition by the loss of the acetonitrile ligand in solution [35], which does commonly not cause problems during ligand-exchange procedures. Likewise, there are also no reports about defined side-products when  $[\text{Tc}(\text{NO})\text{Cl}_2(\text{PPh}_3)_2(\text{CH}_3\text{CN})]$  was used as a precursor.



**Scheme 1.** Syntheses of  $[\text{Tc}(\text{NO})\text{Cl}_2(\text{PPh}_3)_2(\text{CH}_3\text{CN})]$  [35] and  $[\text{Tc}(\text{NO})\text{Cl}_3(\text{OPPh}_3)_2]$ .

Surprisingly, the molecular structure of this important precursor of the nitrosyl technetium chemistry has not been elucidated by X-ray diffraction, as the structure of the analogous rhenium(I) compound  $[\text{Re}(\text{NO})\text{Cl}_2(\text{PPh}_3)_2(\text{CH}_3\text{CN})]$ . During our (less successful) attempts to conduct ligand exchange, starting from **1** with  $(2\text{-pyE})_2$  ligands (as in Figure 1) in acetonitrile, we isolated some pale orange-yellow crystals of  $[\text{Tc}(\text{NO})\text{Cl}_2(\text{PPh}_3)_2(\text{CH}_3\text{CN})]$ , which allowed us to derive basic information about the molecular structure of the complex, such as the composition of the coordination sphere and the arrangement. Unfortunately, the quality of the available single crystals was low; thus, the quality of the derived data was limited. Consequently, they shall not be used here to discuss details of the coordination polyhedron or bond lengths and angles, which are given in the Supplementary Materials and can be inspected there. The coordination positions of the ligands in the environment of technetium and other basic information, however, can doubtlessly be derived and are shown in Figure 2a. The molecular structure of compound **1** is unexceptional, with a distorted octahedral coordination environment around technetium. The nitrosyl ligand is roughly linear, as in all previously studied nitrosyl complexes of technetium [35–41] and shall, thus, be regarded as a formally  $\text{NO}^+$  ligand. This is in good agreement with the diamagnetism of the compound and the  $\nu_{\text{NO}}$  stretch in the IR spectrum at  $1721\text{ cm}^{-1}$  [35]. The acetonitrile ligand binds in an equatorial coordination position *cis* to the nitrosyl ligand. This results in a

bonding situation, as found in the similar rhenium complexes  $[\text{Re}(\text{NO})\text{Cl}_2(\text{PR}_3)_2(\text{CH}_3\text{CN})]$  ( $\text{R} = \text{Me}$ , cyclohexyl, tolyl) [42,43]. The crystal structure of the analogous triphenylphosphine complex  $[\text{Re}(\text{NO})\text{Cl}_2(\text{PPh}_3)_2(\text{CH}_3\text{CN})]$  has not yet been reported.

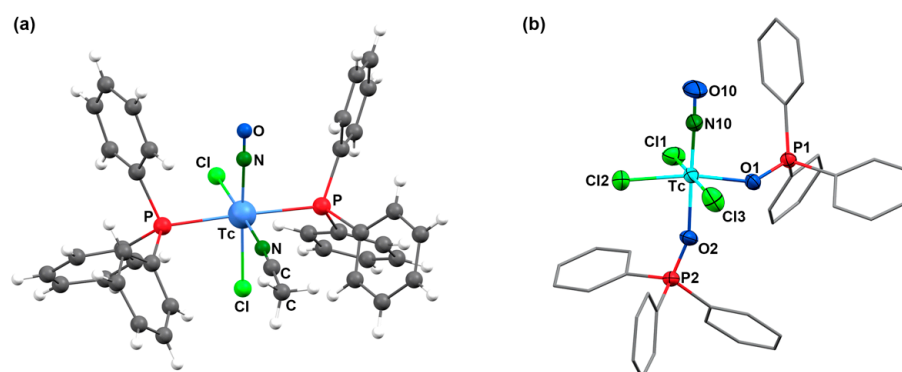


**Figure 2.** (a) Ball and stick representation of the molecular structures of  $[\text{Tc}(\text{NO})\text{Cl}_2(\text{PPh}_3)_2(\text{CH}_3\text{CN})]$  (**1**) and (b) ellipsoid plot of the structure of  $[\text{Tc}(\text{NO})\text{Cl}_3(\text{OPPh}_3)_2]$  (**2**). Thermal ellipsoids represent a 30 percent probability. For color codes, see the atomic labeling scheme.

As previously mentioned,  $[\text{Tc}(\text{NO})\text{Cl}_2(\text{PPh}_3)_2(\text{CH}_3\text{CN})]$  (**1**) is a facile starting material for reactions with a variety of ligand systems, and special precautions are not required as long as the incoming ligands are reactive enough. In the case of less reactive ligands, however, the use of an inert atmosphere is strongly recommended since the formation of phosphine oxide complexes cannot be excluded. This has been proven by a prolonged heating of **1** in toluene in air. The sparingly soluble starting compound gradually dissolved in boiling toluene to give a dark purple solution. After a refluxing period of 5 h, an almost clear solution was obtained, from which a purple solid was deposited upon cooling. Single crystals of  $[\text{Tc}(\text{NO})\text{Cl}_3(\text{OPPh}_3)_2]$  (**2**) were obtained by slow evaporation of the filtered mother solution. The identity of the crystals with the bulk solid was checked by their IR and EPR spectra. In the technetium(II) complex **2**, the  $\nu_{\text{NO}}$  stretch appears at a clearly higher frequency ( $1798\text{ cm}^{-1}$ ) than in compound **1**, as a result of the lower degree of back-donation into the antibonding  $\pi^*$  orbitals of the  $\text{NO}^+$  ligand.

$[\text{Tc}(\text{NO})\text{Cl}_3(\text{OPPh}_3)_2]$  crystallizes as toluene solvate in the monoclinic space group  $P2_1/n$  with two crystallographically-independent species in the asymmetric unit. The molecular structure of **2** is depicted in Figure 2, and some selected bond lengths and angles are compared to the values of complex **1** in Table 1. One of the triphenylphosphine oxide ligands is coordinated *trans* to the nitrosyl ligand, while the other one is in a plane with the three chlorido ligands. The Tc–O bond lengths are very similar with values between 2.070(4) and 2.086(4) Å, which indicates that the multiple-bonded nitrosyl ligand in the technetium(II) complex **2** does not cause a significant *trans* influence. A similar behavior is observed for the Tc–Cl bonds of the diamagnetic  $d^6$  complex **1**. The Tc–O–P bonds in complex **2** are bent as is usual for the coordinated triphenylphosphine oxide ligands. The P–O bond lengths (1.490(4) to 1.507(4) Å) reflect the common double-bond character.

The technetium ion in the Tc(II) complex  $[\text{Tc}(\text{NO})\text{Cl}_3(\text{OPPh}_3)_2]$  (**2**) has a  $d^5$  low-spin configuration with one unpaired electron, which allows the measurement of resolved EPR spectra in liquid and frozen solutions. They show well-resolved hyperfine couplings with the  $^{99}\text{Tc}$  nucleus.  $^{99}\text{Tc}$  has a nuclear spin of  $I = 9/2$ , which causes typical 10-line patterns. Figure 3 shows the spectra of a  $\text{CHCl}_3$  solution of compound **2** at room temperature (a) and at  $T = 77\text{ K}$  (b). The frozen-solution spectrum indicates axial symmetry, resulting in two 10-line patterns each in the parallel and the perpendicular parts of the spectrum.

**Table 1.** Selected bond lengths (Å) and angles (°) in [Tc(NO)Cl<sub>3</sub>(OPPh<sub>3</sub>)<sub>2</sub>] (2) <sup>(a)</sup>.

Tc–N10	1.753(6) 1.842(6)	N10–O10	1.109(6) 0.932(7)	Tc–Cl1	2.370(2) 2.357(2)	Tc–Cl2	2.335(2) 2.265(3)	Tc–Cl3	2.349(2) 2.366(2)
Tc–O1	2.070(4) 2.082(4)	O1–P1	1.490(4) 1.492(4)	Tc–O2	2.086(4) 2.073(4)	O2–P2	1.487(4) 1.507(4)	Tc–N10–O10	177.7(6) 177.2(10)
Tc–O1–P1	143.9(3) 146.7(3)	Tc–O2–P2	159.8(3) 148.3(2)						

<sup>(a)</sup> Values for two independent species. For details, including the individual labelling scheme, see the Supplementary Materials.

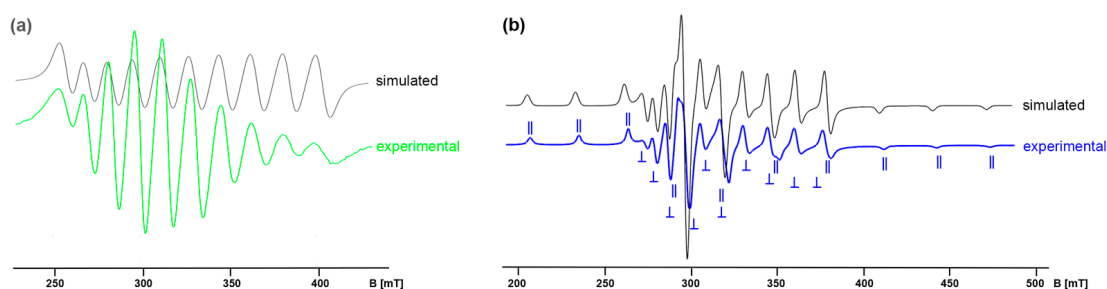


**Figure 3.** EPR spectra of [Tc(NO)Cl<sub>3</sub>(OPPh<sub>3</sub>)<sub>2</sub>] (2) in CHCl<sub>3</sub>: (a) at room temperature and (b) in frozen solution at  $T = 77$  K (|| indicates the lines of the parallel part; ⊥ indicates the lines of the perpendicular part of the spectrum).

The experimental spectrum of Figure 3b can be described by the spin Hamiltonian (1), where  $g_{||}$ ,  $g_{\perp}$ ,  $A_{||}^{\text{Tc}}$ , and  $A_{\perp}^{\text{Tc}}$  are the principal values of the <sup>99</sup>Tc hyperfine tensor  $A^{\text{Tc}}$ . All other expressions have their usual meaning.

$$\hat{H}_{sp} = \beta_e \left[ g_{||} B_z \hat{S}_z + g_{\perp} (B_x \hat{S}_x + B_y \hat{S}_y) \right] + A_{||}^{\text{Tc}} \hat{S}_z \hat{I}_z + A_{\perp}^{\text{Tc}} (\hat{S}_x \hat{I}_x + \hat{S}_y \hat{I}_y) \quad (1)$$

Couplings to the <sup>14</sup>N nucleus of the axial nitrosyl ligand are expectedly small and are not resolved. This is in good agreement with the EPR spectra of all previously studied nitrosyltechnetium(II) compounds. The same holds true for potential couplings to <sup>31</sup>P nuclei of the OPPh<sub>3</sub> ligands. They should be very small since no direct Tc–P bonds are established (see Figure 2). The experimental EPR values obtained for [Tc(NO)Cl<sub>3</sub>(OPPh<sub>3</sub>)<sub>2</sub>] are summarized in Table 2 and compared to the corresponding data of a few other Tc(II) nitrosyl or thionitrosyl complexes with phosphine and/or phosphine oxide ligands. In the first column of the Table, the compositions of the equatorial coordination spheres of the complexes are indicated. It should be noted that the MO of the unpaired electron has mainly ‘xy-character’, which means that the EPR parameters are mainly determined by the donor atoms of the equatorial plane.

**Table 2.** EPR parameters of [Tc(NO)Cl<sub>3</sub>(OPPh<sub>3</sub>)<sub>2</sub>] (3) together with the values of some other Tc(NO) and Tc(NS) complexes. Coupling constants are given in 10<sup>−4</sup> cm<sup>−1</sup>.

Compound		$g_0$	$a_0^{\text{Tc}}$	$g_{  }$	$g_{\perp}$	$A_{  }^{\text{Tc}}$	$A_{\perp}^{\text{Tc}}$	$A_{  }^{\text{P}}$	Ref.
[Tc(NO)Cl <sub>3</sub> (OPPh <sub>3</sub> ) <sub>2</sub> ] (2)	(Cl <sub>3</sub> O) <sup>(a)</sup>	2.0291	152	1.9750	2.0320	273	110	-	This work
[Tc(NO)Br <sub>3</sub> (OPPh <sub>3</sub> ) <sub>2</sub> ]	(Br <sub>3</sub> O) <sup>(a)</sup>	2.056	148	2.042	2.059	237	100	-	[44]
[Tc(NO)Cl <sub>3</sub> (PMe <sub>2</sub> Ph) <sub>2</sub> ]	(Cl <sub>2</sub> P <sub>2</sub> ) <sup>(a)</sup>	2.045	125	2.034	2.053	215	88	19 <sup>(b)</sup>	[45]
[Tc(NO)Br <sub>3</sub> (PMe <sub>2</sub> Ph) <sub>2</sub> ]	(Br <sub>2</sub> P <sub>2</sub> ) <sup>(a)</sup>	2.108	111	2.119	2.100	184	79	-	[45]
[Tc(NS)Cl <sub>3</sub> (PPh <sub>3</sub> ) <sub>2</sub> ]	(Cl <sub>2</sub> P <sub>2</sub> ) <sup>(a)</sup>	2.011	164	1.955	2.0455	270	128	-	[46]
[Tc(NS)Cl <sub>3</sub> (PPh <sub>3</sub> )(OPPh <sub>3</sub> )]	(Cl <sub>3</sub> P) <sup>(a)</sup>	2.009	166	1.978	1.999	290	134	-	[46]
[Tc(NS)Cl <sub>3</sub> (PMe <sub>2</sub> Ph) <sub>2</sub> ]	(Cl <sub>2</sub> P <sub>2</sub> ) <sup>(a)</sup>	2.045	133	2.027	2.038	219	101	19 <sup>(b)</sup>	[47]
[Tc(NS)Cl <sub>3</sub> (PMe <sub>2</sub> Ph)(OPMe <sub>2</sub> Ph)]	(Cl <sub>3</sub> P) <sup>(a)</sup>	2.032	149	2.027	2.039	237	106	24 <sup>(c)</sup>	[48]

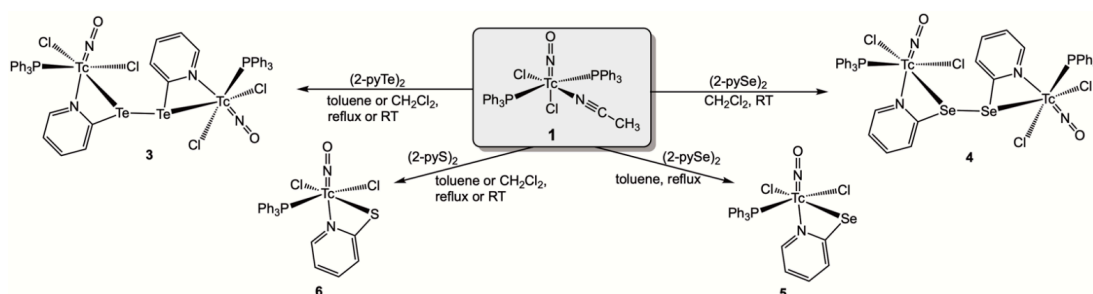
<sup>(a)</sup> Composition of the equatorial coordination sphere, <sup>(b)</sup> Triplet, <sup>(c)</sup> Doublet.

Compound **2** of the present study is indeed only the second nitrosyl or thionitrosyl technetium(II) complex with a phosphine oxide ligand in its equatorial coordination sphere. Its bromido analog  $[\text{Tc}(\text{NO})\text{Br}_3(\text{OPPh}_3)_2]$  has been formed during attempts to oxidize the cyclopentadienyl compound  $[\text{Tc}(\text{NO})(\text{Cp})\text{Br}(\text{PPh}_3)]$  with elemental bromine [44]. A comparison of the EPR parameters, listed in Table 1, indicates a general increase in  $^{99}\text{Tc}$  hyperfine couplings when phosphine ligands are replaced by phosphine oxides. This can be understood by a lower degree of delocalization of electron density into the ligand orbitals of oxygen donors and is not unusual for axially-symmetric technetium(II) complexes. In a similar way, the influence of the halide ligands on the spectral parameters can be explained, where the transfer of some electron density in the orbitals of bromido or iodido ligands could be proven experimentally, while such effects are much smaller for chlorido ligands [49–51].

The formation of the phosphine oxide complex **2** is, in a way, reversible, in that the addition of excess  $\text{PPh}_3$  and  $\text{HCl}$  to a solution of **2** in acetonitrile results in the reduction and reconstitution of  $[\text{Tc}(\text{NO})\text{Cl}_2(\text{PPh}_3)_2(\text{CH}_3\text{CN})]$ . Thus, the detected formation of **2** during ligand exchange procedures starting from **1** does not present a considerable problem, which also applies to reactions of the technetium(I) precursor with 2,2'-dipyridyl dichalcogenides used in the present study.

## 2.2. Reactions of $[\text{Tc}(\text{NO})\text{Cl}_2(\text{PPh}_3)_2(\text{CH}_3\text{CN})]$ (**1**) with 2,2'-Dipyridyl Dichalcogenides

The composition of the complexes formed upon treatment of compound **1** with (2-pyE)<sub>2</sub> ligands depends on the chalcogen E and the reaction conditions applied. Only one product could be isolated with (2-pyTe)<sub>2</sub>, the dark blue, binuclear compound  $[\{\text{Tc}(\text{NO})\text{Cl}_2(\text{PPh}_3)_2\}_2\{\mu_2\text{-}(2\text{-pyTe})_2\}]$  (**3**), which is only sparingly soluble and immediately precipitated from  $\text{CH}_2\text{Cl}_2$  (room temperature reaction) or from boiling toluene. A similar product,  $[\{\text{Tc}(\text{NO})\text{Cl}_2(\text{PPh}_3)_2\}_2\{\mu_2\text{-}(2\text{-pySe})_2\}]$  (**4**), was obtained during a room-temperature reaction with the corresponding diselenide, while a reduction of (2-pySe)<sub>2</sub> was observed during prolonged reaction times or at elevated temperatures. The newly formed 2-pyridylselenolate acts as a chelating ligand and forms the technetium(II) complex  $[\text{Tc}(\text{NO})\text{Cl}_2(\text{PPh}_3)(2\text{-pySe})]$  (**5**). An analogous compound,  $[\text{Tc}(\text{NO})\text{Cl}_2(\text{PPh}_3)(2\text{-pyS})]$  (**6**), is the sole product of the reaction of **1** with (2-pyS)<sub>2</sub>, irrespective of the reaction conditions. Attempts to isolate a corresponding technetium(I) product with intact disulfide failed, even at  $-20\text{ }^\circ\text{C}$ . Scheme 2 contains a summary of the successful reactions.



**Scheme 2.** Reactions of  $[\text{Tc}(\text{NO})\text{Cl}_2(\text{PPh}_3)_2(\text{CH}_3\text{CN})]$  with 2,2'-dipyridyl dichalcogenides and the structures of the products.

The coordination mode of the (2-pyE)<sub>2</sub> ligands in compound **3** and **4** with two *N*,*Te* or *N*,*Se* donor sets bridging two metal ions is without precedence. Most of the hitherto studied metal complexes with 2,2'-dipyridyl dichalcogenides concern the respective disulfides and most of the metal ions are bonded exclusively via the nitrogen atoms of the ligands [21]. Such a bonding mode is also found in a number of complexes with (2-pySe)<sub>2</sub> [19,27–29] or (2-pyTe)<sub>2</sub> [31,33,34]. Chelate formation involving the chalcogen atoms has only been

observed in exceptional cases and commonly results in tridentate *N,E,N* coordination to one metal ion [31,34,52]. Only three compounds are known in which such ligands act as bridges between two metal atoms, and in none of them have two *N,E* chelates been established [31,34,53]. This, however, is the case in the technetium complexes **3** and **4**. The molecular structures of the two compounds are depicted in Figure 4, and selected bond lengths and angles are provided in Table 3.

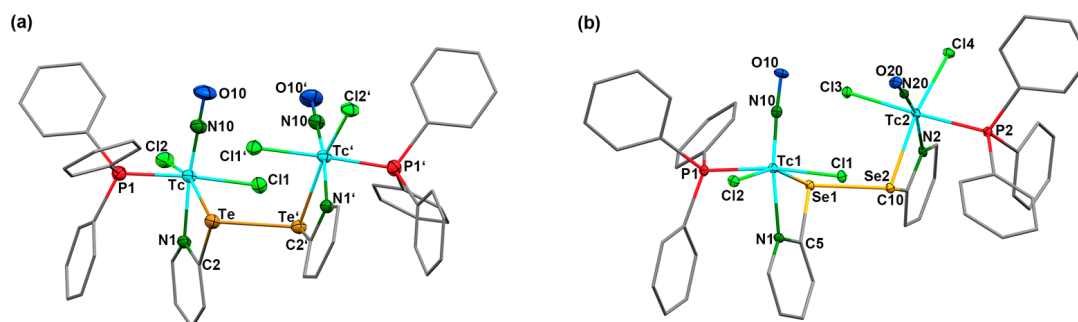


**Figure 4.** Molecular structures of (a)  $[\{\text{Tc}(\text{NO})\text{Cl}_2(\text{PPh}_3)_2\{\mu_2\text{-(2-pyTe)}_2\}]$  (**3**) and (b)  $[\{\text{Tc}(\text{NO})\text{Cl}_2(\text{PPh}_3)_2\{\mu_2\text{-(2-pySe)}_2\}]$  (**4**). Thermal ellipsoids represent a 30 percent probability. For color code see the atomic labelling scheme.

**Table 3.** Selected bond lengths (Å) and angles (°) in  $[\{\text{Tc}(\text{NO})\text{Cl}_2(\text{PPh}_3)_2\{\mu_2\text{-(2-pyTe)}_2\}]$  (**3**) and  $[\{\text{Tc}(\text{NO})\text{Cl}_2(\text{PPh}_3)_2\{\mu_2\text{-(2-pySe)}_2\}]$  (**4**).

Compound 3 <sup>(a)</sup>							
Tc–N10	1.734(4)	N10–O10	1.184(5)	Tc–Cl1	2.463(1)	Tc–Cl2	2.416(1)
Tc–P1	2.390(1)	Tc–Te	2.6587(5)	Tc–N1	2.181(3)	Te–Te′	2.8319(6)
Tc...Tc′	5.199(2)	Tc–N10–O10	179.5(5)	Te–Tc–N1	70.72(8)	N1–C2–Te	105.8(3)
Compound 4							
Tc1–N10	1.742(4)	N10–O10	1.197(5)	Tc1–Cl1	2.443(1)	Tc1–Cl2	2.410(1)
Tc1–P1	2.404(1)	Tc1–Se1	2.4730(6)	Tc2–N20	1.743(4)	N20–O20	1.189(5)
Tc2–Cl3	2.446(1)	Tc2–Cl4	2.409(1)	Tc2–P2	2.395(1)	Tc2–Se2	2.4663(6)
Tc2–N2	2.195(4)	Se1–Se2	2.5491(7)	Tc1...Tc2	5.109(2)	Tc1–N10–O10	176.5(4)
Se1–Tc1–N1	69.9(1)	Tc1–N10–O10	176.7(4)	Se2–Tc2–N2	69.8(1)	N1–C5–Se1	108.0(3)
N2–C10–Se2	107.8(4)						

<sup>(a)</sup> Symmetry operation:  $x, 1 - y, 3/2 - z$ .

Complexes **3** and **4** are the first examples of technetium complexes with ditelluride or diselenide ligands. The coordination spheres of the technetium atoms are distorted octahedra. This is mainly due to the limiting bite angles inside the four-membered chelate rings, which cause significant deviations from the ideal 90° and 180° angles inside the respective *N,Cl,N,Te/Se* coordination planes. The torsion angles around the chalcogen-chalcogen bonds of the coordinated (2-pyE)<sub>2</sub> ligands are 85.0° for the ditelluride and 90.6° for the diselenide. The planes of the pyridine rings are twisted by approximately 25°. With regard to the Tc–Tc distances of >5.1 Å in compounds **3** and **4**, no interactions between the technetium atoms can be assumed.

Generally, there are only a few structurally characterized compounds with technetium-tellurium [54] or technetium-selenium bonds [54–57]. The Tc–Te/Se bond lengths found in **3** and **4** are in the range of those in the  $[\text{Tc}^{\text{V}}\text{O}(\text{PhE})_4]^-$  anions (E = Te: 2.662 Å, E = Se: 2.473 Å) [54]. Slightly shorter bonds have been found in 5-coordinate technetium(III) complexes of the composition  $[\text{Tc}(\text{PPh}_3)_2(\text{aryLE})_3]$  [54], and clearly longer Tc–Se bonds

(2.637–2.654 Å) are reported for technetium(I) complexes with selenoether and selenourea ligands [55]. Interestingly, the formation of the  $Te,N$  and  $Se,N$  chelates has a marked influence on the central Te–Te and Se–Se bonds. Their bond lengths increase upon coordination by approximately 0.16 Å (Te complex) and 0.25 Å (Se compound) compared to the values of the uncoordinated dichalcogenides [28,58–60]. The suggested weakening of these bonds as a result of the coordination to technetium is discussed as part of the theoretical investigation using density functional theory (DFT) in a later section of this study. It is remarkable that the lengthening of these bonds is more pronounced for the selenium compound and may help to understand the observed formation of a second product,  $[Tc(NO)Cl_2(PPh_3)(2-pySe)]$  (**5**), during reactions of  $[Tc(NO)Cl_2(PPh_3)_2(CH_3CN)]$  with  $(2-pySe)_2$ , which is observed at harsher reaction conditions. Compound **5** precipitates from the reaction mixture in refluxing toluene as a fairly stable green powder. It is a technetium(II) complex, as could be proven by the measured IR and EPR spectra (vide infra). Solutions of **5** slowly decompose. Thus, we were not yet able to grow single crystals of this compound for X-ray diffraction. The spectroscopic data, however, strongly support a structure in analogy to the corresponding thiolato complex **6**.

$[Tc(NO)Cl_2(PPh_3)(2-pyS)]$  (**6**) is formed in good yields upon treatment of  $[Tc(NO)Cl_2(PPh_3)_2(CH_3CN)]$  (**1**) with  $(2-pyS)_2$ . Reduction of the disulfide is observed even at room temperature and there was no evidence for the formation of an intermediate with a coordinated disulfide. Green single crystals of compound **6** were obtained from a  $CH_2Cl_2$ /toluene mixture. The molecular structure of the products is shown in Figure 5; selected bond lengths and angles are summarized in Table 4.

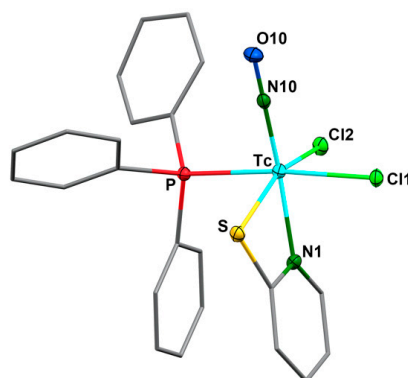


**Figure 5.** Molecular structure of  $[Tc(NO)Cl_2(PPh_3)(2-pyS)]$  (**6**). Thermal ellipsoids represent a 30 percent probability. For color code see the atomic labelling scheme.

**Table 4.** Selected bond lengths (Å) and angles (°) in  $[Tc(NO)Cl_2(PPh_3)(2-pyS)]$  (**6**).

Tc–N10	1.754(2)	N10–O10	1.176(3)	Tc–Cl1	2.4129(7)
Tc–Cl2	2.390(1)	Tc–P	2.4642(7)	Tc–S	2.345(2)
Tc–N1	2.140(2)	Tc–N10–O10	177.0(2)	S–Tc–N1	68.94(7)

The exclusive formation of a technetium(II) complex during a reaction starting from the Tc(I) precursor  $[Tc(NO)Cl_2(PPh_3)_2(CH_3CN)]$  might be regarded as a result of the ready reduction of the disulfide since simple ligand-exchange reactions of the similar starting material  $[Tc(NO)Cl_2(PPh_3)_2(CH_3OH)]$  with 2-pyridinethiol retains the metals oxidation state, exclusively forming the Tc(I) compounds  $[Tc(NO)Cl(PPh_3)_2(2-pyS)]$  and  $[Tc(NO)(PPh_3)_2(2-pyS)]$  [61]. The arrangement of the  $(2-pyS)^-$  ligand in the technetium(I) products with the nitrogen donor in *trans*-position to  $NO^+$  is also found in compound **6**. There are also no significant differences in the bond lengths. The linear nitrosyl unit with a Tc–N–O angle of 177.0(2)° is in agreement with the treatment as  $NO^+$ , which is also confirmed by the IR spectroscopic data.

The  $\nu_{\text{NO}}$  stretches of Tc(I) complexes **3** and **4** appear between 1722 and 1753  $\text{cm}^{-1}$ , while those of the Tc(II) products **5** and **6** are found at 1778 and 1782  $\text{cm}^{-1}$ . The differences are due to the larger degree of backdonation into antibonding ligand orbitals in the technetium(I) complexes with a  $d^6$  electronic configuration. The diamagnetism of the Tc(I) compounds allows the recording of NMR spectra including the  $^{99}\text{Tc}$  resonances.  $^{99}\text{Tc}$  is a remarkable NMR nucleus with a nuclear spin of  $I = 9/2$  and a high relative molar receptivity *versus*  $^1\text{H}$  of approximately 0.4 [62]. This allows for the detection of small differences in the coordination sphere of diamagnetic technetium complexes. A significant drawback is the strong influence of the molecular symmetry on the linewidth of the  $^{99}\text{Tc}$  NMR signals due to the large quadrupole moment of this nucleus, which results in line widths between some 100 Hz and several kHz. A partial compensation for this inconvenience is given by the extremely large spectral range in which  $^{99}\text{Tc}$  NMR signals appear. Figure 6a illustrates the situation for the complexes **3** and **4**. Although they are only sparingly soluble, they are chemically very similar, and, as their  $^{99}\text{Tc}$  NMR line widths are in the range of 2000 Hz, they can readily be recorded with a sufficient signal/noise ratio. They appear at clearly different chemical shifts. The latter fact allows the use of this method to monitor chemical reactions between diamagnetic species and helps to predict the composition of the contributing species. Suitable  $^{31}\text{P}$  NMR signals could not be resolved for compounds **3** and **4**, which is a frequent feature for compounds with Tc–P bonds and commonly explained by a strong line-broadening due to scalar couplings between  $^{31}\text{P}$  and the large quadrupole moment of  $^{99}\text{Tc}$  [46].

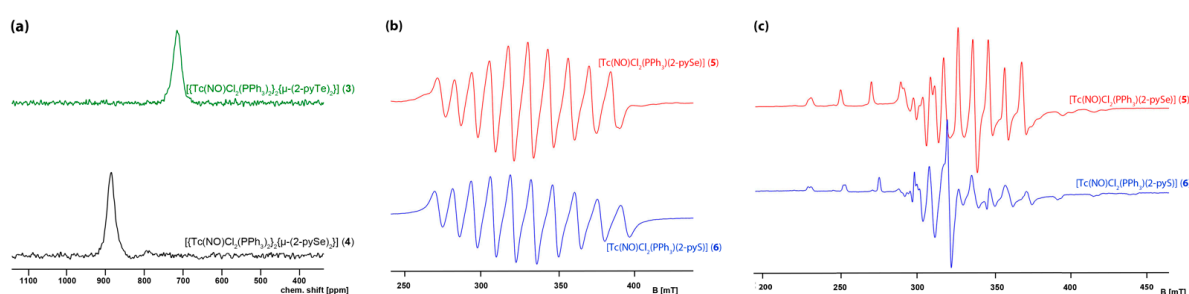


**Figure 6.** (a)  $^{99}\text{Tc}$  NMR spectra of  $[\{\text{Tc}(\text{NO})\text{Cl}_2(\text{PPh}_3)_2\}_2\{\mu_2\text{-(2-pyTe)}_2\}]$  (**3**) and  $[\{\text{Tc}(\text{NO})\text{Cl}_2(\text{PPh}_3)_2\}_2\{\mu_2\text{-(2-pySe)}_2\}]$  (**4**), (b) room-temperature EPR spectra in  $\text{CHCl}_3$  of  $[\text{Tc}(\text{NO})\text{Cl}_2(\text{PPh}_3)_2(2\text{-pySe})]$  (**5**) ( $g_0 = 2.0315$ ;  $a_0^{\text{Tc}} = 119 \times 10^{-4} \text{ cm}^{-1}$ ) and  $[\text{Tc}(\text{NO})\text{Cl}_2(\text{PPh}_3)_2(2\text{-pyS})]$  (**6**) ( $g_0 = 2.0225$ ;  $a_0^{\text{Tc}} = 126 \times 10^{-4} \text{ cm}^{-1}$ ), and (c) frozen-solution EPR spectra in  $\text{CHCl}_3$  of **5** ( $g_{\parallel} = 2.0850$ ,  $g_{\perp} = 2.0265$ ;  $A_{\parallel}^{\text{Tc}} = 199 \times 10^{-4} \text{ cm}^{-1}$ ,  $A_{\perp}^{\text{Tc}} = 86 \times 10^{-4} \text{ cm}^{-1}$ ,  $A_{\parallel}^{\text{P}} = 20 \times 10^{-4} \text{ cm}^{-1}$ ,  $A_{\perp}^{\text{P}} = 18 \times 10^{-4} \text{ cm}^{-1}$ ) and **6** ( $g_{\parallel} = 2.0650$ ,  $g_{\perp} = 2.0265$ ;  $A_{\parallel}^{\text{Tc}} = 150 \times 10^{-4} \text{ cm}^{-1}$ ,  $A_{\perp}^{\text{Tc}} = 86 \times 10^{-4} \text{ cm}^{-1}$ ,  $A_{\parallel}^{\text{P}} = 15 \times 10^{-4} \text{ cm}^{-1}$ ,  $A_{\perp}^{\text{P}} = 9 \times 10^{-4} \text{ cm}^{-1}$ ).

In contrast, compounds **5** and **6** are paramagnetic technetium(II) compounds with a  $d^5$  ‘low-spin’ configuration. The resulting  $S = 1/2$  system allows for the detection of well-resolved solution EPR spectra at ambient temperatures. They are compared in Figure 6. The expected 10-line pattern due to couplings of the unpaired electron with the nuclear spin of  $^{99}\text{Tc}$  ( $I = 9/2$ ) is clearly seen in their liquid solution spectra (Figure 6b). Two sets of ten lines are found in frozen solution spectra of the compounds confirming the ‘axial symmetry’ of the spectra, as has been described for compound **2** *vide supra*, and a similar spin Hamiltonian (2) can be applied for the description of the spectra. Since the coordination spheres of the technetium atoms in **5** and **6** contain phosphine ligands, which establish couplings with the unpaired electron, the corresponding  $^{31}\text{P}$  superhyperfine interactions must be considered.

$$\hat{H}_{sp} = \beta_e \left[ g_{\parallel} B_z \hat{S}_z + g_{\perp} (B_x \hat{S}_x + B_y \hat{S}_y) \right] + A_{\parallel}^{\text{Tc}} \hat{S}_z \hat{I}_z + A_{\perp}^{\text{Tc}} (\hat{S}_x \hat{I}_x + \hat{S}_y \hat{I}_y) + \sum SA^{\text{P}} I^{\text{P}} \quad (2)$$



A comparison of the experimental spectra and the derived parameters (see Figure 6) gives a general trend. The ‘replacement’ of a sulfur donor atom in the equatorial coordination sphere by a selenium atom results in a clear decrease of the  $^{99}\text{Tc}$  couplings, which means that more electron density is transferred to ligand orbitals. DFT calculations on the B3LYP-GD3B/StuttgartRSC(Tc)/StuttgartRLC+STO-3G(Te)/6-31G\*(C,N,P,Cl)/6-31G(H) level indicate that the SOMO orbitals in the paramagnetic Tc(II) monomers are indeed spread over technetium, the chalcogen, the nitrosyl ligand, and the organic pyridyl backbone, while the spin density shows a localization of the unpaired electron at technetium with only slight delocalization onto the nitrosyl ligand. The calculated MO of the unpaired electron is in good agreement with the experimental findings and the only small couplings with the  $^{31}\text{P}$  nuclei of the phosphine ligands in compounds **5** and **6** (Figure 6c). A visualization of the relevant orbitals can be found in the Supplementary Materials.

The conducted experiments, the spectral data and the structural parameters confirm clear differences between the two technetium(I) complexes **3** and **4** and between the technetium(II) complexes **5** and **6**. The selenium compounds represent a kind of link concerning the spectral parameters and the observed reactivity. Although no direct or quantitative information can be derived from the observed bond lengthening of the Te–Te and Se–Se bonds during the formation of compounds **3** and **4**, a double one electron transfer from each Tc(I) ion to the adjacent chalcogen atom in the dichalcogenide can be assumed for the observed bond cleavage and the generation of the  $\{2\text{-pySe}\}^-$  and  $\{2\text{-pyS}\}^-$  ligands. To get more insights into the electronic situation of the complexes, we conducted some studies with computational methods.

### 2.3. DFT Calculations

To rationalize the observed reactivity and the discrepancy in the behavior of the different dichalcogenides, density functional theory (DFT) calculations were performed on the B3LYP level in the gas phase. Better thermochemical parameters were derived based on calculations at the B3LYP-GD3BJ level that were additionally corrected for low-energy rotational modes (see Section 3 for details).

On all levels of theory, the relative trend for the oxidation of technetium and the reduction of the dichalcogenide was  $\text{Te} < \text{Se} < \text{S}$ , which is in perfect agreement with the experimental observations. On the higher level calculations, including a solvent model and dispersion correction, it becomes evident that the ditelluride technetium(I) complex **3** is an irreversible thermodynamic sink with an energetic preference of ca. 50 kJ/mol, while, for the selenium compounds, the energy difference allows for an equilibrium between monomeric Tc(II) selenolate and dimeric Tc(I) diselenide. These findings are consistent with the observations made for both Tc(I) and Tc(II) compounds depending on the conditions ( $\Delta\Delta G \approx 10$  kJ/mol). For the disulfide, the dissociation under the internal redox reaction between S and Tc is favored by ca. 40 kJ/mol, which is in full agreement with the formation of the thiolato complex **6** as the sole product during the reactions conducted. The homolytic cleavage of the E–E bonds in the free dichalcogenides is energetically severely disfavored in all cases, indicating that the metal coordination plays a crucial role in the symmetric dissociation. Interestingly, the lowest barrier is even encountered for the dissociation of the Te–Te bond, which agrees with chemical intuition and highlights the contrast to the metal-mediated reaction described herein in both experiment and theory.

The theoretical widening of the E–E bond upon coordination of the corresponding dichalcogenide to technetium is  $2.13 \text{ \AA} \rightarrow 2.56 \text{ \AA}$  ( $\Delta(\text{S})_{\text{DFT}} = 0.43 \text{ \AA}$ ),  $2.49 \text{ \AA} \rightarrow 2.78 \text{ \AA}$  ( $\Delta(\text{Se})_{\text{DFT}} = 0.29 \text{ \AA}$ ), and  $2.83 \text{ \AA} \rightarrow 2.98 \text{ \AA}$  ( $\Delta(\text{Te})_{\text{DFT}} = 0.15 \text{ \AA}$ ), which is in close agreement with the experimentally observed values of  $\Delta(\text{Te})_{\text{exp}} = 0.16 \text{ \AA}$  and  $\Delta(\text{Se})_{\text{exp}} = 0.25 \text{ \AA}$ . Interestingly, this behavior of the present system represents a unique opportunity to verify the

influence of the coordination in two different dichalcogenides with the otherwise same general structure. The observed widening of the E–E bond is consistent with a prediction made for the metal-induced reduction of dichalcogenides by the normally not sufficiently reducing, but intrinsically released, triphenylphosphine ligands upon coordination of the dichalcogenide to group 7 or group 10 metals [63–65]. As calculated for palladium species, the chalcogen-chalcogen bond is weakened due to a polarization of the chalcogen-chalcogen bond upon coordination, with the metal-coordinated chalcogen atom becoming partially more negative, while the non-coordinated chalcogen atom shows a significantly increased  $\sigma$ -hole, which makes the E–E bond more prone to the nucleophilic attack of the incoming phosphine, reducing agent forming metal chalcogenolato complexes [65]. The corresponding electrostatic potential (ESP) maps of the dichalcogenides and their technetium complexes are provided as Supplementary Materials; however, the effect of the increased  $\sigma$ -hole is masked by a compression of the structures due to increased interaction of the suitably positioned chloride donor atoms on the  $\sigma$ -hole of the chalcogens. Nevertheless, the bond length deviations are strong evidence for the suggested mechanistic concept of ref. [65].

The experimental  $^{99}\text{Tc}$  NMR data of compounds **3** and **4** have been used to optimize and test a DFT approach for the prediction of corresponding chemical shifts; for details, see a previous report [66]. The experimental and calculated data are in good agreement (for compound **3**: 716 vs. 703 ppm, for compound **4**: 883 vs. 989 ppm), also keeping in mind that simple solvent effects may cause chemical shift differences up to 100 ppm in the large scale of  $^{99}\text{Tc}$  chemical shifts of several thousand ppm.

The HOMO and LUMO orbitals in the dimers correspond to a technetium-centered d-orbital and to the anti-bonding  $\sigma^*$  orbital of the chalcogen-chalcogen single-bond, respectively, in all cases. The corresponding situation is visualized for the ditelluride complex **3** in Figure 7. Analogous Figures for the other compounds are given as Supplementary Materials.

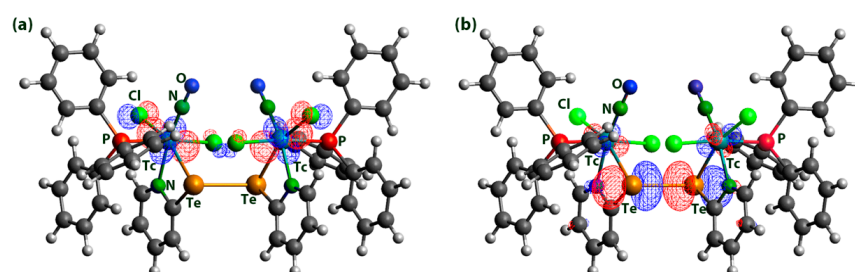


**Figure 7.** (a) HOMO and (b) LUMO of  $[\{\text{Tc}^{\text{I}}(\text{NO})\text{Cl}_2(\text{PPh}_3)_2\}_2\{\mu_2\text{-[2-pyTe]}_2\}]$  at an isosurface value of 0.05 at the B3LYP-GD3B/StuttgartRSC(Tc)/StuttgartRLC+STO-3G(Te)/6-31G\*(C,N,P,Cl)/6-31G(H) level. For color code, see the atomic labelling scheme.

As the compounds are intensely colored, time-dependent (TD-) DFT calculations were used to simulate the UV-Vis spectra of the compounds and to verify the presence of monomeric Tc(II) for S and Se, while dimeric Tc(I) is observed for Te (see Supplementary Materials). The observed band maxima and spectral shapes are in good agreement with the experimental spectra. The lowest energy absorption band of the Tc(II) compounds shows a bathochromic shift from S to Te, while a hypsochromic shift of the lowest energy visible absorption band is observed from S to Te in the Tc(I) compounds. Thus,  $[\{\text{Tc}^{\text{I}}(\text{NO})\text{Cl}_2(\text{PPh}_3)_2\}_2\{\mu_2\text{-[2-pyTe]}_2\}]$  is deep blue as its highest absorption wavelength is lowered into the range of 650 nm compared to  $[\{\text{Tc}^{\text{I}}(\text{NO})\text{Cl}_2(\text{PPh}_3)_2\}_2\{\mu_2\text{-[2-pyE]}_2\}]$  (E = S, Se). In comparison, a two-band-pattern with absorptions at ca. 450 nm and 700–750 nm in the UV-Vis spectra of  $[\text{Tc}(\text{NO})\text{Cl}_2(\text{PPh}_3)(2\text{-pyE})]$  (E = S, Se) leads to the observed green color.

The experimental  $^{99}\text{Tc}$  NMR data of compounds **3** and **4** have been used to test a DFT approach for the prediction of corresponding chemical shifts; for details, see a

previous report [66]. The experimental and calculated data are in good agreement (for compound 3: 716 vs. 703 ppm, for compound 4: 883 vs. 989 ppm), also keeping in mind that simple solvent effects may cause chemical shift differences up to 100 ppm in the large scale of  $^{99}\text{Tc}$  chemical shifts of several thousand ppm.

### 3. Materials and Methods

Unless otherwise stated, reagent-grade solvents and starting materials were used. Solvents were dried and distilled prior to use. Inert conditions were only applied when explicitly mentioned.  $[\text{Tc}(\text{NO})\text{Cl}_2(\text{PPh}_3)_2(\text{CH}_3\text{CN})]$  [35],  $(2\text{-pyTe})_2$  [34], and  $(2\text{-pySe})_2$  [67] were prepared according to literature procedures.

#### 3.1. Radiation Precaution

All synthetic work with technetium was performed in a laboratory approved for the handling of radioactive material. All personnel working in this project were permanently monitored for potential contaminations.

#### 3.2. Physical Measurements

IR spectra were measured as KBr pellets on a Shimadzu IR Affinity-1 spectrometer (Shimadzu, Kyoto, Japan). NMR spectra were recorded on JEOL 400 MHz spectrometers (JEOL, Kyoto, Japan). X-Band EPR spectra were recorded in solution with a Magnettech Miniscope MS400 spectrometer (Magnettech, Berlin, Germany) at 300 and 78 K. Simulation and visualization of the EPR spectra were done with the EasySpin toolbox in MatLab (Version: 24.2.0) [68,69].

#### 3.3. Syntheses

$[\text{Tc}(\text{NO})\text{Cl}_3(\text{OPPh}_3)_2]$  (2).  $[\text{Tc}(\text{NO})\text{Cl}_2(\text{PPh}_3)_2(\text{CH}_3\text{CN})]$  (1) (76 mg, 0.1 mmol) was suspended in toluene (5 mL) and heated under reflux for 5 h in air. The insoluble starting material slowly dissolved and a dark solution was formed. A dark purple solid precipitated upon cooling and purple single crystals formed upon slow evaporation of the residual solution. Yield: 60% (47 mg). IR (KBr,  $\text{cm}^{-1}$ ): 3425(m), 3056(w), 2918(w), 1798(vs)  $\nu_{\text{NO}}$ , 1589(w), 1437(s), 1319(m), 1175(m)  $\nu_{\text{PO}}$ , 1159(m)  $\nu_{\text{PO}}$ , 1123(vs)  $\nu_{\text{PO}}$ , 1080(s), 1120(m), 1026(m), 997(m), 752(m), 727(vs), 692(s), 623(w), 536(s), 471(w). EPR (RT,  $\text{CHCl}_3$ ):  $g_0 = 2.0291$ ;  $a_0^{\text{Tc}} = 152 \times 10^{-4} \text{ cm}^{-1}$ . EPR (77 K,  $\text{CHCl}_3$ ):  $g_{\parallel} = 1.9750$ ,  $g_{\perp} = 2.0320$ ;  $A_{\parallel}^{\text{Tc}} = 273 \times 10^{-4} \text{ cm}^{-1}$ ,  $A_{\perp}^{\text{Tc}} = 110 \times 10^{-4} \text{ cm}^{-1}$ .

$[\{\text{Tc}(\text{NO})\text{Cl}_2(\text{PPh}_3)_2\}_2\{\mu\text{-}(2\text{-pyTe})_2\}]$  (3). (a)  $(2\text{-pyTe})_2$  (50 mg, 0.13 mmol) was dissolved in  $\text{CH}_2\text{Cl}_2$  (3 mL) and added to a suspension of  $[\text{Tc}(\text{NO})\text{Cl}_2(\text{PPh}_3)_2(\text{CH}_3\text{CN})]$  (1) (76 mg, 0.1 mmol) in  $\text{CH}_2\text{Cl}_2$  (3 mL). The mixture was stirred at room temperature for 3 h. A gradual dissolution of the starting material and the formation of a deep-blue solution was observed, from which a blue solid started to precipitate. The solution was filtered, and toluene (2 mL) was added to the filtrate. Slow evaporation of the solvents resulted in the formation of blue single crystals for X-ray diffraction. The crystalline product was identical to the blue powder, which separated from the reaction mixture in the first step, as could be proven by IR, NMR, and UV/vis measurements. Overall yield: 49 mg (74%). (b)  $(2\text{-pyTe})_2$  (50 mg, 0.13 mmol) was dissolved in 2 mL toluene and added to a suspension of  $[\text{Tc}(\text{NO})\text{Cl}_2(\text{PPh}_3)_2(\text{CH}_3\text{CN})]$  (1) (76 mg, 0.1 mmol) in toluene (2 mL). The mixture was heated under reflux for 1 h. A deep-blue solid gradually precipitated from the reaction mixture during the reflux period. More product was obtained upon cooling. It was filtered off and recrystallized from  $\text{CH}_2\text{Cl}_2$ /toluene. Yield: 37 mg (55%). IR (KBr,  $\text{cm}^{-1}$ ): 3433(s), 3037(w), 2968(w), 2920(w), 1753(vs)  $\nu_{\text{NO}}$ , 1561(w), 1497(w), 1436(s), 1271(m), 1157(w), 1091(m), 1041(w), 1026(w), 748(m), 696(s), 522(s).  $^1\text{H-NMR}$  ( $\text{CD}_2\text{Cl}_2$ , ppm): 8.24 (d, 2H, py),

7.62–7.75 (m, 2H, py), 7.48–7.45 (m, 2H, py), 7.30–7.26 (m, 6H, PPh<sub>3</sub>), 7.09–7.26 (m, 24H, PPh<sub>3</sub>) 6.96–6.93 (m, 2H, py). <sup>99</sup>Tc-NMR (CD<sub>2</sub>Cl<sub>2</sub>, ppm): 716 ( $\nu_{1/2}$  = 2200 Hz). UV/Vis (CH<sub>2</sub>Cl<sub>2</sub>,  $\lambda_{\max}$ , nm,  $\epsilon$ ): 444, 2863 cm<sup>-1</sup>mol<sup>-1</sup>.

[[Tc(NO)Cl<sub>2</sub>(PPh<sub>3</sub>)<sub>2</sub>][ $\mu$ -(2-pySe)<sub>2</sub>]] (4). (2-pySe)<sub>2</sub> (40 mg, 0.13 mmol) was dissolved in CH<sub>2</sub>Cl<sub>2</sub> (3 mL) and added to a suspension of [Tc(NO)Cl<sub>2</sub>(PPh<sub>3</sub>)<sub>2</sub>(CH<sub>3</sub>CN)] (1) (76 mg, 0.1 mmol) in CH<sub>2</sub>Cl<sub>2</sub> (3 mL). The mixture was stirred at room temperature for 3 h. A gradual dissolution of the starting material was observed. The solution was filtered, and toluene (2 mL) was added to the filtrate. Slow evaporation of the solvents resulted in the formation of red-brown single crystals, which were suitable for X-ray diffraction. Yield: 22 mg (35%). More product could be isolated from the mother liquor. This, however, contained significant amounts of the Tc(II) product 5. Analytical data have been determined for the crystalline product 4. IR (KBr, cm<sup>-1</sup>): 3428(s), 3049(w), 2968(w), 1722 (vs)  $\nu_{\text{NO}}$ , 1562(m), 1497(w), 1436(s), 1414(s) 1186(m), 1117(m), 754(m), 721(m), 694(s), 542(s), 522(m). <sup>1</sup>H-NMR (CD<sub>2</sub>Cl<sub>2</sub>, ppm): 8.24 (d, 2H, py), 7.62–7.75 (m, 2H, py), 7.48–7.45 (m, 2H,py), 7.30–7.26 (m, 6H, PPh<sub>3</sub>), 7.09–7.26 (m, 24H, PPh<sub>3</sub>) 6.96–6.93 (m, 2H, py). <sup>99</sup>Tc-NMR (CD<sub>2</sub>Cl<sub>2</sub>, ppm): 885 ( $\nu_{1/2}$  = 1940 Hz). UV/Vis (CH<sub>2</sub>Cl<sub>2</sub>,  $\lambda_{\max}$ , nm,  $\epsilon$ ): 476, 3002 cm<sup>-1</sup>mol<sup>-1</sup>, 768, 2442 cm<sup>-1</sup>mol<sup>-1</sup>.

[Tc(NO)Cl<sub>2</sub>(PPh<sub>3</sub>)(2-pySe)] (5): [Tc(NO)Cl<sub>2</sub>(PPh<sub>3</sub>)<sub>2</sub>(CH<sub>3</sub>CN)] (76 mg, 0.1 mmol) was suspended in toluene (4 mL) and (2-pySe)<sub>2</sub> (14 mg, 0.13 mmol) was added dissolved in 4 mL toluene. The mixture was heated under reflux for 90 min, filtered, and allowed to cool to room temperature. A small amount of a green powder was deposited upon slow evaporation of the dark brown solution. Yield: 15 mg (22%). More of compound 5 was contained in the remaining solution, as was confirmed by EPR and IR spectroscopy. This extra amount, however, could not be isolated in an analytically pure form due to impurities of 4 and a second paramagnetic Tc(II) product. Analytical data have been determined for the crystalline product 5. IR (KBr, cm<sup>-1</sup>): 3426(m), 3053(w), 2922(m), 2852(w), 1778(s)  $\nu_{\text{NO}}$ , 1584(s), 1444(vs), 1416(vs), 1266(w), 1192(s), 1119(s), 754(s), 721(s), 688(s), 542(vs). EPR (RT, CHCl<sub>3</sub>):  $g_0$  = 2.0315;  $a_0^{\text{Tc}}$  = 119 × 10<sup>-4</sup> cm<sup>-1</sup>. EPR (77 K, CHCl<sub>3</sub>):  $g_{\parallel}$  = 2.0850,  $g_{\perp}$  = 2.0265;  $A_{\parallel}^{\text{Tc}}$  = 199 × 10<sup>-4</sup> cm<sup>-1</sup>,  $A_{\perp}^{\text{Tc}}$  = 86 × 10<sup>-4</sup> cm<sup>-1</sup>,  $A_{\parallel}^{\text{P}}$  = 20 × 10<sup>-4</sup> cm<sup>-1</sup>,  $A_{\perp}^{\text{P}}$  = 18 × 10<sup>-4</sup> cm<sup>-1</sup>.

[Tc(NO)Cl<sub>2</sub>(PPh<sub>3</sub>)(2-pyS)] (6): (a) (2-pyS)<sub>2</sub> (28 mg, 0.13 mmol) was dissolved in CH<sub>2</sub>Cl<sub>2</sub> (3 mL) and added to a suspension of [Tc(NO)Cl<sub>2</sub>(PPh<sub>3</sub>)<sub>2</sub>(CH<sub>3</sub>CN)] (1) (76 mg, 0.1 mmol) in CH<sub>2</sub>Cl<sub>2</sub> (3 mL). The mixture was stirred at room temperature for 3 h. A gradual dissolution of the starting material and the formation of a green solution was observed. The solution was filtered and toluene (2 mL) was added to the filtrate. Slow evaporation of the solvents resulted in the formation of green single crystals for X-ray diffraction. Yield: 48 mg (85%). (b) The same product was obtained when the reaction was performed in refluxing toluene (1 h). Yield: 43 mg (75%). IR (KBr, cm<sup>-1</sup>): 3068(w), 1759(vs)  $\nu_{\text{NO}}$ , 1585(w), 1481(w), 1433(s), 1271(m), 1134(w), 1097(m), 1090(w), 997(w), 764(m), 746(s), 729(s), 694(s), 525(m), 513(m), 497(m), 443(w). EPR (RT, CHCl<sub>3</sub>):  $g_0$  = 2.0225;  $a_0^{\text{Tc}}$  = 126 × 10<sup>-4</sup> cm<sup>-1</sup>. EPR (77 K, CHCl<sub>3</sub>):  $g_{\parallel}$  = 2.0650,  $g_{\perp}$  = 2.0265;  $A_{\parallel}^{\text{Tc}}$  = 150 × 10<sup>-4</sup> cm<sup>-1</sup>,  $A_{\perp}^{\text{Tc}}$  = 86 × 10<sup>-4</sup> cm<sup>-1</sup>,  $A_{\parallel}^{\text{P}}$  = 15 × 10<sup>-4</sup> cm<sup>-1</sup>,  $A_{\perp}^{\text{P}}$  = 9 × 10<sup>-4</sup> cm<sup>-1</sup>. UV/Vis (CH<sub>2</sub>Cl<sub>2</sub>,  $\lambda_{\max}$ , nm,  $\epsilon$ ): 462, 2051 cm<sup>-1</sup>mol<sup>-1</sup>, 698, 3650 cm<sup>-1</sup>mol<sup>-1</sup>.

### 3.4. X-Ray Crystallography

The intensities for the X-ray determinations were collected on a Bruker CCD instrument (BRUKER, Billerica, MA, USA) with Mo/K $\alpha$  radiation. Semi-empirical absorption corrections were carried out by SADABS [70]. Structure solution and refinement were performed with the SHELX programs [71,72] included in the OLEX2 program package [73].

Hydrogen atoms were calculated for idealized positions and treated with the 'riding model' option of SHELXL. The solvent mask option of OLEX2 was applied to treat diffuse electron density due to disordered solvents. Details are given in the Supplementary Materials. The representation of molecular structures was conducted using the program Mercury [74].

### 3.5. Computational Chemistry

DFT calculations were performed on the high-performance computing systems of the Freie Universität Berlin ZEDAT (Curta) using the program package GAUSSIAN 16 Rev. A.03 [75]. The gas phase geometry optimizations in vacuum were performed using coordinates derived from the X-ray crystal structures or were modeled with the use of crystal structure fragments using GAUSSVIEW [76], while initial guesses for calculations involving an implicit polarizable continuum model with integral equation formalism (IEF-PCM) for the solvent toluene were derived from the gas phase optimized structures [77]. The gas phase calculations were performed by using the hybrid density functional B3LYP [78–80], while the solution phase calculations were empirically corrected for dispersion by Grimme's D3 method with Becke-Johnson damping [81]. The relativistic small-core basis set Stuttgart RSC 1997, with the respective effective core potential (ECP), was applied to Tc [82,83]. The Stuttgart relativistic large-core basis set augmented by STO-3G polarization functions was applied to S, Se, and Te, together with the respective ECPs [84–87]. The standard all-electron basis set 6-31G\* was applied to C, N, P, and Cl [88–90]. The 6-31G basis set was applied for all other atoms [91]. The hybrid functional B3LYP was chosen based on robustness and with regard to a compromise between computational cost and reliable geometry optimization. Although relativistic effects should be small for Tc, as stated in the original benchmarking of the basic constituents of the Stuttgart basis set and ECP, the relativistic small core basis set was proven as a robust yet versatile basis set for Tc in B3LYP (see, e.g., [66,92–95]). For all other atoms, the choice of basis functions was a compromise between size/accuracy and computational time, and, although the results do not differ much, we preferably use the bigger LANL2DZ for donor atoms directly coordinated to technetium due to its increased accuracy. NMR tensors were calculated for the B3LYP-level optimized gas-phase structures using the B3P86 functional [78,96] combined with the dedicated all-electron NMR basis set x2c-TZVPPall-s for all atoms [97]. Similar approaches have recently been suggested; however, such methods commonly revolved around the exact replication of experimental chemical shifts by exact modeling of solvent, relativistic, and quadrupolar effects with methods of high computational cost and expert knowledge requirements [98–104], whereas the presented approach of using low-cost functionals combined with low-cost modern basis sets is of much lower computational cost could allow a routine implementation to complement experimental studies by non-experts after an in-depth benchmarking. Such benchmarking is currently ongoing, and a corresponding manuscript is in preparation. All basis sets and ECPs were obtained from the basis set exchange database [105].

The convergence of the optimized geometries was verified by frequency calculations. The absence of negative frequencies characterizes the obtained geometries as energetic minima. Convergence criteria for the frequency calculations: Maximum Force 0.00045; RMS Force 0.00030; Maximum Displacement 0.0018; RMS Displacement 0.0012. Often, the region on the energy hypersurface was very flat for the present systems, so, sometimes, the convergence of single parameters was not tightly adhered to, and structures showing neglectable predicted changes in energy ( $<2 \times 10^{-7}$  Hartree) were accepted as converged structures if no imaginary frequencies were obtained. The entropic [106] and enthalpic [107] contributions of low-energy modes to the free energy were corrected using the quasi-harmonic approximation of Grimme, as implemented in the freely accessible Python code GoodVibes of Funes-Ardoiz and Paton with a cut-off at  $500 \text{ cm}^{-1}$  [108].

Further analysis of the obtained wave functions was done using MultiWFN [109]. Visualization of orbitals was done using GAUSSVIEW [76] or Avogadro [110]. A method for the estimation of NMR chemical shifts was taken from ref. [66].

#### 4. Conclusions

When exposed to the technetium(I) complex  $[\text{Tc}(\text{NO})\text{Cl}_2(\text{PPh}_3)_2(\text{CH}_3\text{CN})]$ , 2,2'-Dipyridyl ditelluride, 2,2'-dipyridyl diselenide, and 2,2'-dipyridyl disulfide show clear differences in their reactivity. While reduction of the disulfide and the exclusive formation of the technetium(II) complex  $[\text{Tc}(\text{NO})\text{Cl}_2(\text{PPh}_3)(2\text{-pyS})]$  is observed, technetium(I) complexes with intact dichalcogenides are isolated during reactions with the corresponding diselenide and ditelluride. Interestingly, the chalcogen-chalcogen bonds in the complexes are widened in the complexes compared with those in the uncoordinated pro-ligands. This effect is more significant for the diselenide, which is in accord with the observed reactivity since this bond is cleaved when the reaction is conducted under elevated temperatures and a Tc(II) compound with the corresponding selenolate is formed. The experimental findings are supported by DFT calculation, which suggests a clear contribution of the back-donation of electron density into antibonding orbitals of the coordinated dichalcogenides, which are located in the corresponding E–E bonds.

Although derived for complexes of the artificial element technetium, the experimental findings might have implications for the explanation of slight differences observed for thiolate/disulfide and selenolate/diselenide couples in biological systems and/or during the development of pharmaceuticals, branches which enter more and more the focus of interest in the current research field [111–115].

**Supplementary Materials:** The following supporting information can be downloaded at: <https://www.mdpi.com/article/10.3390/molecules30040793/s1>: Table S1. Crystallographic data and data collection parameters. Figure S1. Ellipsoid representation of the structure of  $[\text{Tc}(\text{NO})\text{Cl}_2(\text{PPh}_3)_2(\text{CH}_3\text{CN})]$  (1). The thermal ellipsoids are set at a 30% probability level. Hydrogen atoms bonding to carbon atoms are omitted for clarity. Table S2. Bond lengths (Å) in  $[\text{Tc}(\text{NO})\text{Cl}_2(\text{PPh}_3)_2(\text{CH}_3\text{CN})]$  (1). Table S3. Bond angles (°) in  $[\text{Tc}(\text{NO})\text{Cl}_2(\text{PPh}_3)_2(\text{CH}_3\text{CN})]$  (1). Figure S2. Ellipsoid representation of the structure of  $[\{\text{Tc}(\text{NO})\text{Cl}_2(\text{PPh}_3)_2\{\mu_2\text{-}(2\text{-pyTe})_2\}]$  (3)  $\times$   $\text{CH}_2\text{Cl}_2$   $\times$  2 toluene (removed by a solvent mask due to an extended disorder). The thermal ellipsoids are set at a 30% probability level. Hydrogen atoms are omitted for clarity. Table S4. Bond lengths (Å) in  $[\{\text{Tc}(\text{NO})\text{Cl}_2(\text{PPh}_3)\{\mu_2\text{-pyTeTepy}\}]$   $\times$   $\text{CH}_2\text{Cl}_2$ . Table S5. Bond angles (°) in  $[\{\text{Tc}(\text{NO})\text{Cl}_2(\text{PPh}_3)_2\{\mu_2\text{-}(2\text{-pyTe})_2\}]$  (3)  $\times$   $\text{CH}_2\text{Cl}_2$ . Figure S3. Ellipsoid representation of  $[\{\text{Tc}(\text{NO})\text{Cl}_2(\text{PPh}_3)_2\{\mu_2\text{-}(2\text{-pySe})_2\}]$  (4)  $\times$  1.5 toluene. The thermal ellipsoids are set at a 30% probability level. Hydrogen atoms are omitted for clarity. Table S6. Bond lengths (Å) in  $[\{\text{Tc}(\text{NO})\text{Cl}_2(\text{PPh}_3)_2\{\mu_2\text{-}(2\text{-pySe})_2\}]$  (4)  $\times$  1.5 toluene. Table S7. Bond angles (°) in  $[\{\text{Tc}(\text{NO})\text{Cl}_2(\text{PPh}_3)_2\{\mu_2\text{-}(2\text{-pySe})_2\}]$  (4)  $\times$  1.5 toluene. Figure S4. Ellipsoid representation of the complexes contained in  $[\text{Tc}^{\text{II}}(\text{NO})\text{Cl}_2(\text{PPh}_3)(2\text{-pyS})]$  (6)  $\times$  0.5 toluene, also illustrating disorders in the  $\text{PyS}^-$  ligand, two of the phenyl rings and the solvent toluene. The thermal ellipsoids are set at a 30% probability level. Hydrogen atoms are omitted for clarity. Table S8. Bond lengths (Å) in  $[\text{Tc}^{\text{II}}(\text{NO})\text{Cl}_2(\text{PPh}_3)(2\text{-pyS})]$  (6)  $\times$  0.5 toluene. Table S9. Bond angles (°) in  $[\text{Tc}^{\text{II}}(\text{NO})\text{Cl}_2(\text{PPh}_3)(2\text{-pyS})]$  (6)  $\times$  0.5 toluene. Figure S5. IR spectrum (KBr) of  $[\text{Tc}(\text{NO})\text{Cl}_3(\text{OPPh}_3)_2]$  (2). Figure S6. Room-temperature EPR spectrum of  $[\text{Tc}(\text{NO})\text{Cl}_3(\text{OPPh}_3)_2]$  (2) in  $\text{CHCl}_3$ . Figure S7. Frozen-solution EPR spectrum ( $T = 78$  K) of  $[\text{Tc}(\text{NO})\text{Cl}_3(\text{OPPh}_3)_2]$  (2) in  $\text{CHCl}_3$ . Figure S8. IR spectrum (KBr) of  $[\{\text{Tc}^{\text{I}}(\text{NO})\text{Cl}_2(\text{PPh}_3)_2\{\mu_2\text{-}(2\text{-pyTe})_2\}]$  (3). Figure S9.  $^1\text{H}$  NMR spectra of  $[\{\text{Tc}^{\text{I}}(\text{NO})\text{Cl}_2(\text{PPh}_3)_2\{\mu_2\text{-}(2\text{-pyTe})_2\}]$  (3) in  $\text{CD}_2\text{Cl}_2$ . Figure S10.  $^{99}\text{Tc}$  and  $^{31}\text{P}$  NMR (not visible) spectra of  $[\{\text{Tc}^{\text{I}}(\text{NO})\text{Cl}_2(\text{PPh}_3)_2\{\mu_2\text{-}(2\text{-pyTe})_2\}]$  (3) in  $\text{CD}_2\text{Cl}_2$ . Figure S11. Normalized experimental UV-Vis spectrum of  $[\{\text{Tc}^{\text{I}}(\text{NO})\text{Cl}_2(\text{PPh}_3)_2\{\mu_2\text{-}(2\text{-pyTe})_2\}]$ . Figure S12. IR spectrum (KBr) of  $[\{\text{Tc}^{\text{I}}(\text{NO})\text{Cl}_2(\text{PPh}_3)_2\{\mu_2\text{-}(2\text{-pySe})_2\}]$  (4). Figure S13.  $^1\text{H}$  NMR spectra of  $[\{\text{Tc}^{\text{I}}(\text{NO})\text{Cl}_2(\text{PPh}_3)_2\{\mu_2\text{-}(2\text{-pySe})_2\}]$  (4) in  $\text{DMSO-D}_6$ . Figure S14.  $^{99}\text{Tc}$  spectrum of  $[\{\text{Tc}^{\text{I}}(\text{NO})\text{Cl}_2(\text{PPh}_3)_2\{\mu_2\text{-}(2\text{-pySe})_2\}]$  (4)  $\text{DMSO-D}_6$ . Figure S15. Normalized experimental UV-Vis spectrum of  $[\text{Tc}^{\text{II}}(\text{NO})\text{Cl}_2(\text{PPh}_3)(2\text{-pyS})]$  (6)  $\times$  0.5 toluene.

pySe)]. Figure S16. IR spectrum (KBr) of  $[\text{Tc}(\text{NO})\text{Cl}_2(\text{PPh}_3)(2\text{-pySe})]$ . Figure S17. Room-temperature X-band EPR spectrum of  $[\text{Tc}(\text{NO})\text{Cl}_2(\text{PPh}_3)(2\text{-pySe})]$  in  $\text{CHCl}_3$ . Figure S18. Frozen-solution ( $T = 77\text{ K}$ ) X-band EPR spectrum of  $[\text{Tc}(\text{NO})\text{Cl}_2(\text{PPh}_3)(2\text{-pySe})]$  in  $\text{CHCl}_3$ . Figure S19. IR spectrum (KBr) of  $[\text{Tc}(\text{NO})\text{Cl}_2(\text{PPh}_3)(2\text{-pyS})]$ . Figure S20. Room-temperature X-band EPR spectrum of  $[\text{Tc}(\text{NO})\text{Cl}_2(\text{PPh}_3)(2\text{-pyS})]$  in  $\text{CHCl}_3$ . Figure S21. Frozen-solution ( $T = 77\text{ K}$ ) X-band EPR spectrum of  $[\text{Tc}(\text{NO})\text{Cl}_2(\text{PPh}_3)(2\text{-pyS})]$  in  $\text{CHCl}_3$ . Figure S22. Normalized experimental UV-Vis spectrum of  $[\text{Tc}^{\text{II}}(\text{NO})\text{Cl}_2(\text{PPh}_3)(2\text{-pyS})]$ . Figure S23. HOMO of  $[\{\text{Tc}^{\text{I}}(\text{NO})\text{Cl}_2(\text{PPh}_3)\}_2\{\mu_2\text{-}(2\text{-pyS})_2\}]$  at an isosurface value of 0.05. B3LYP-GD3B/StuttgartRSC(Tc)/StuttgartRLC+STO-3G(S)/6-31G\*(C,N,P,Cl)/6-31G(H) level. Figure S24. LUMO of  $[\{\text{Tc}^{\text{I}}(\text{NO})\text{Cl}_2(\text{PPh}_3)\}_2\{\mu_2\text{-}(2\text{-pyS})_2\}]$  at an isosurface value of 0.05. B3LYP-GD3B/StuttgartRSC(Tc)/StuttgartRLC+STO-3G(S)/6-31G\*(C,N,P,Cl)/6-31G(H) level. Figure S25. Comparison between experimental UV-Vis spectrum of  $[\{\text{Tc}^{\text{I}}(\text{NO})\text{Cl}_2(\text{PPh}_3)\}_2\{\mu_2\text{-}(2\text{-pyTe})_2\}]$  and simulated UV-Vis spectra of the (hypothetical) monomeric  $[\text{Tc}^{\text{II}}(\text{NO})\text{Cl}_2(\text{PPh}_3)(2\text{-pyTe})]$  or dimeric  $[\{\text{Tc}^{\text{I}}(\text{NO})\text{Cl}_2(\text{PPh}_3)\}_2\{\mu_2\text{-}(2\text{-pyTe})_2\}]$ ; 50 transitions were respectively considered (indicated by lines). B3LYP-GD3B/StuttgartRSC(Tc)/StuttgartRLC+STO-3G(Te)/6-31G\*(C,N,P,Cl)/6-31G(H) level. The spectral signature in the visible part of the spectrum is consistent with the presence of the dimeric Tc(I) instead of the (hypothetical) monomeric Tc(II) compound. Figure S26. Spin density of  $[\text{Tc}(\text{NO})\text{Cl}_2(\text{PPh}_3)(2\text{-pyS})]$  at an isosurface level of 0.01. B3LYP-GD3B/StuttgartRSC(Tc)/StuttgartRLC+STO-3G(S)/6-31G\*(C,N,P,Cl)/6-31G(H) level. Figure S27. SOMO of  $[\text{Tc}(\text{NO})\text{Cl}_2(\text{PPh}_3)(2\text{-pyS})]$ . B3LYP-GD3B/StuttgartRSC(Tc)/StuttgartRLC+STO-3G(S)/6-31G\*(C,N,P,Cl)/6-31G(H) level. Figure S28. LUMO of  $[\text{Tc}(\text{NO})\text{Cl}_2(\text{PPh}_3)(2\text{-pyS})]$ . B3LYP-GD3B/StuttgartRSC(Tc)/StuttgartRLC+STO-3G(S)/6-31G\*(C,N,P,Cl)/6-31G(H) level. Figure S29. Comparison between experimental UV-Vis spectrum of  $[\text{Tc}^{\text{II}}(\text{NO})\text{Cl}_2(\text{PPh}_3)(2\text{-pyS})]$  and simulated UV-Vis spectra of the monomeric  $[\text{Tc}^{\text{II}}(\text{NO})\text{Cl}_2(\text{PPh}_3)(2\text{-pyS})]$  or (hypothetic) dimeric  $[\{\text{Tc}^{\text{I}}(\text{NO})\text{Cl}_2(\text{PPh}_3)\}_2\{\mu_2\text{-}(2\text{-pyS})_2\}]$ ; 50 transitions were respectively considered (indicated by lines). B3LYP-GD3B/StuttgartRSC(Tc)/StuttgartRLC+STO-3G(S)/6-31G\*(C,N,P,Cl)/6-31G(H) level. The spectral signature in the visible part of the spectrum is consistent with the presence of the monomeric Tc(II) instead of the (hypothetical) dimeric Tc(I) compound. Figure S30. HOMO of  $[\{\text{Tc}^{\text{I}}(\text{NO})\text{Cl}_2(\text{PPh}_3)\}_2\{\mu_2\text{-}(2\text{-pySe})_2\}]$  at an isosurface value of 0.05. B3LYP-GD3B/StuttgartRSC(Tc)/StuttgartRLC+STO-3G(Se)/6-31G\*(C,N,P,Cl)/6-31G(H) level. Figure S31. LUMO of  $[\{\text{Tc}^{\text{I}}(\text{NO})\text{Cl}_2(\text{PPh}_3)\}_2\{\mu_2\text{-}(2\text{-pySe})_2\}]$  at an isosurface value of 0.05. B3LYP-GD3B/StuttgartRSC(Tc)/StuttgartRLC+STO-3G(Se)/6-31G\*(C,N,P,Cl)/6-31G(H) level. Figure S32. Comparison between experimental UV-Vis spectrum of  $[\text{Tc}^{\text{II}}(\text{NO})\text{Cl}_2(\text{PPh}_3)(2\text{-pySe})]$  and simulated UV-Vis spectra of the monomeric  $[\text{Tc}^{\text{II}}(\text{NO})\text{Cl}_2(\text{PPh}_3)(2\text{-pySe})]$  or dimeric  $[\{\text{Tc}^{\text{I}}(\text{NO})\text{Cl}_2(\text{PPh}_3)\}_2\{\mu_2\text{-}(2\text{-pySe})_2\}]$ ; 50 transitions were respectively considered (indicated by lines). B3LYP-GD3B/StuttgartRSC(Tc)/StuttgartRLC+STO-3G(Se)/6-31G\*(C,N,P,Cl)/6-31G(H) level. The spectral signature in the visible part of the spectrum is consistent with the presence of the monomeric Tc(II) instead of the dimeric Tc(I) compound. Figure S33. Spin density of  $[\text{Tc}(\text{NO})\text{Cl}_2(\text{PPh}_3)(2\text{-pySe})]$  at an isosurface level of 0.01. B3LYP-GD3B/StuttgartRSC(Tc)/StuttgartRLC+STO-3G(Se)/6-31G\*(C,N,P,Cl)/6-31G(H) level. Figure S34. SOMO of  $[\text{Tc}(\text{NO})\text{Cl}_2(\text{PPh}_3)(2\text{-pySe})]$ . B3LYP-GD3B/StuttgartRSC(Tc)/StuttgartRLC+STO-3G(Se)/6-31G\*(C,N,P,Cl)/6-31G(H) level. Figure S35. LUMO of  $[\text{Tc}(\text{NO})\text{Cl}_2(\text{PPh}_3)(2\text{-pySe})]$ . B3LYP-GD3B/StuttgartRSC(Tc)/StuttgartRLC+STO-3G(Se)/6-31G\*(C,N,P,Cl)/6-31G(H) level. Figure S36. Simulated UV-Vis spectrum of  $[\text{Tc}(\text{NO})\text{Cl}_2(\text{PPh}_3)(2\text{-pySe})]$ ; 50 transitions were considered. B3LYP-GD3B/StuttgartRSC(Tc)/StuttgartRLC+STO-3G(Se)/6-31G\*(C,N,P,Cl)/6-31G(H) level. Figure S37. HOMO of  $[\{\text{Tc}^{\text{I}}(\text{NO})\text{Cl}_2(\text{PPh}_3)\}_2\{\mu_2\text{-}(2\text{-pyTe})_2\}]$  at an isosurface value of 0.05. B3LYP-GD3B/StuttgartRSC(Tc)/StuttgartRLC+STO-3G(Te)/6-31G\*(C,N,P,Cl)/6-31G(H) level. Figure S38. LUMO of  $[\{\text{Tc}^{\text{I}}(\text{NO})\text{Cl}_2(\text{PPh}_3)\}_2\{\mu_2\text{-}(2\text{-pyTe})_2\}]$  at an isosurface value of 0.05. B3LYP-GD3B/StuttgartRSC(Tc)/StuttgartRLC+STO-3G(Te)/6-31G\*(C,N,P,Cl)/6-31G(H) level. Figure S39. Simulated UV-Vis spectrum of  $[\{\text{Tc}^{\text{I}}(\text{NO})\text{Cl}_2(\text{PPh}_3)\}_2\{\mu_2\text{-}(2\text{-pyTe})_2\}]$ ; 50 transitions were considered. B3LYP-GD3B/StuttgartRSC(Tc)/StuttgartRLC+STO-3G(S,Te,Te)/6-31G\*(C,N,P,Cl)/6-31G(H) level. Figure S40. Spin density of  $[\text{Tc}(\text{NO})\text{Cl}_2(\text{PPh}_3)(2\text{-pyTe})]$  at an isosurface level of 0.01. B3LYP-GD3B/StuttgartRSC(Tc)/StuttgartRLC+STO-3G(Te)/6-31G\*(C,N,P,Cl)/6-31G(H) level. Figure S41. SOMO of  $[\text{Tc}(\text{NO})\text{Cl}_2(\text{PPh}_3)(2\text{-pyTe})]$ . B3LYP-GD3B/StuttgartRSC(Tc)/StuttgartRLC+STO-3G(Te)/6-31G\*(C,N,P,Cl)/6-31G(H) level. Figure S42. LUMO of  $[\text{Tc}(\text{NO})\text{Cl}_2(\text{PPh}_3)(2\text{-pyTe})]$ . B3LYP-GD3B/StuttgartRSC(Tc)/StuttgartRLC+STO-3G(Te)/6-31G\*(C,

N,P,Cl)/6-31G(H) level. Figure S43. Simulated UV-Vis spectrum of  $[\text{Tc}(\text{NO})\text{Cl}_2(\text{PPh}_3)(2\text{-pyTe})]$ ; 50 transitions were considered. B3LYP-GD3B/StuttgartRSC(Tc)/StuttgartRLC+STO-3G(Te)/6-31G\*(C, N,P,Cl)/6-31G(H) level. Table S10. Free energies  $\Delta G$  obtained by the DFT calculations at different levels (gas-phase: standard conditions, B3LYP/StuttgartRSC(Tc)/StuttgartRLC+STO-3G(Te)/6-31G\*(C,N,P,Cl)/6-31G(H) level; solvent: IEF-PCM for toluene at B3LYP-GD3B/StuttgartRSC(Tc)/StuttgartRLC+STO-3G(Te)/6-31G\*(C,N,P,Cl)/6-31G(H) level & solvent with correction for rotational modes). Table S11. Highest occupied molecular orbital (HOMO or singly occupied molecular orbital; SOMO) and highest unoccupied molecular orbital (LUMO) energies and energy differences. Calculations with IEF-PCM for solvent toluene at B3LYP-GD3B/StuttgartRSC(Tc)/StuttgartRLC+STO-3G(Te)/6-31G\*(C,N,P,Cl)/6-31G(H) level & solvent with correction for rotational modes). Table S12.  $^{99}\text{Tc}$  NMR chemical shifts and shielding tensors calculated at B3P86/x2c-TZVPPall-s level based on geometries calculated with IEF-PCM for solvent toluene at B3LYP-GD3B/StuttgartRSC(Tc)/StuttgartRLC+STO-3G(Te)/6-31G\*(C,N,P,Cl)/6-31G(H) level & solvent with correction for rotational modes). Table S13. Free energies  $\Delta G$  obtained by the DFT calculations for the dissociation of  $(2\text{-pyE})_2$  in toluene (IEF-PCM) at B3LYP-GD3B/StuttgartRSC(Tc)/StuttgartRLC+STO-3G(Te)/6-31G\*(C,N,P,Cl)/6-31G(H) level. Table S14. Highest occupied molecular orbital (HOMO or singly occupied molecular orbital; SOMO) and highest unoccupied molecular orbital (LUMO) energies and energy differences for  $\cdot\{2\text{-pyE}\}$  and  $(2\text{-pyE})_2$ . Calculations with IEF-PCM for solvent toluene at B3LYP-GD3B/StuttgartRSC(Tc)/StuttgartRLC+STO-3G(Te)/6-31G\*(C,N,P,Cl)/6-31G(H) level & solvent with correction for rotational modes). Figure S44. HOMO of  $(2\text{-pyS})_2\text{P}$  at an isosurface value of 0.05. B3LYP-GD3B/StuttgartRSC(Tc)/StuttgartRLC+STO-3G(S)/6-31G\*(C,N,P,Cl)/6-31G(H) level. Figure S45. LUMO of  $(2\text{-pyS})_2$  at an isosurface value of 0.05. B3LYP-GD3B/StuttgartRSC(Tc)/StuttgartRLC+STO-3G(S)/6-31G\*(C,N,P,Cl)/6-31G(H) level. Figure S46. HOMO of  $(2\text{-pySe})_2$  at an isosurface value of 0.05. B3LYP-GD3B/StuttgartRSC(Tc)/StuttgartRLC+STO-3G(Se)/6-31G\*(C,N,P,Cl)/6-31G(H) level. Figure S47. LUMO of  $(2\text{-pyTe})_2$  at an isosurface value of 0.05. B3LYP-GD3B/StuttgartRSC(Tc)/StuttgartRLC+STO-3G(Se)/6-31G\*(C,N,P,Cl)/6-31G(H) level. Figure S48. HOMO of  $(2\text{-pyTe})_2$  at an isosurface value of 0.05. B3LYP-GD3B/StuttgartRSC(Tc)/StuttgartRLC+STO-3G(Te)/6-31G\*(C,N,P,Cl)/6-31G(H) level. Figure S49. LUMO of  $(2\text{-pyTe})_2$  at an isosurface value of 0.05. B3LYP-GD3B/StuttgartRSC(Tc)/StuttgartRLC+STO-3G(Te)/6-31G\*(C,N,P,Cl)/6-31G(H) level. Figure S50. SOMO of  $\cdot\{2\text{-pyS}\}$  at an isosurface value of 0.05. U-B3LYP-GD3B/StuttgartRSC(Tc)/StuttgartRLC+STO-3G(S)/6-31G\*(C,N,P,Cl)/6-31G(H) level. Figure S51. LUMO of  $\cdot\{\text{pyS}\}$  at an isosurface value of 0.05. U-B3LYP-GD3B/StuttgartRSC(Tc)/StuttgartRLC+STO-3G(S)/6-31G\*(C,N,P,Cl)/6-31G(H) level. Figure S52. SOMO of  $\cdot\{2\text{-pySe}\}$  at an isosurface value of 0.05. U-B3LYP-GD3B/StuttgartRSC(Tc)/StuttgartRLC+STO-3G(Se)/6-31G\*(C,N,P,Cl)/6-31G(H) level. Figure S53. LUMO of  $\cdot\{2\text{-pySe}\}$  at an isosurface value of 0.05. U-B3LYP-GD3B/StuttgartRSC(Tc)/StuttgartRLC+STO-3G(Se)/6-31G\*(C,N,P,Cl)/6-31G(H) level. Figure S54. SOMO of  $\cdot\{2\text{-pyTe}\}$  at an isosurface value of 0.05. U-B3LYP-GD3B/StuttgartRSC(Tc)/StuttgartRLC+STO-3G(Te)/6-31G\*(C,N,P,Cl)/6-31G(H) level. Figure S55. LUMO of  $\cdot\{2\text{-pyTe}\}$  at an isosurface value of 0.05. U-B3LYP-GD3B/StuttgartRSC(Tc)/StuttgartRLC+STO-3G(Te)/6-31G\*(C,N,P,Cl)/6-31G(H) level. Figure S56. Spin densities of  $\cdot\{2\text{-pyE}\}$  (left to right; E = S, Se, Te) at an isosurface value of 0.01. U-B3LYP-GD3B/StuttgartRSC(Tc)/StuttgartRLC+STO-3G(S)/6-31G\*(C,N,P,Cl)/6-31G(H) level. Figure S57. Electrostatic potential (ESP) mapping of  $(2\text{-pyS})_2$  at an isosurface value of 0.004 (left: transparent mesh to highlight molecular orientation, right: untransparent mesh to highlight the values). Dark blue: corresponds to a surface potential of  $8.314 \times 10^{-2}$ , while green is 0 and red is  $-8.314 \times 10^{-2}$ . B3LYP-GD3B/StuttgartRSC(Tc)/StuttgartRLC+STO-3G(S)/6-31G\*(C,N,P,Cl)/6-31G(H) level. Figure S58. Electrostatic potential (ESP) mapping of  $(2\text{-pySe})_2$  at an isosurface value of 0.004 (left: transparent mesh to highlight molecular orientation, right: untransparent mesh to highlight the values). Dark blue: corresponds to a surface potential of  $8.314 \times 10^{-2}$ , while green is 0 and red is  $-8.314 \times 10^{-2}$ . The values are normalized to those of free  $(2\text{-pyS})_2$ . B3LYP-GD3B/StuttgartRSC(Tc)/StuttgartRLC+STO-3G(Se)/6-31G\*(C,N,P,Cl)/6-31G(H) level. Figure S59. Electrostatic potential (ESP) mapping of  $(2\text{-pyTe})_2$  at an isosurface value of 0.004 (left: transparent mesh to highlight molecular orientation, right: untransparent mesh to highlight the values). Dark blue: corresponds to a surface potential of  $8.314 \times 10^{-2}$ , while green is 0 and red is  $-8.314 \times 10^{-2}$ . The



values are normalized to those of free (2-pyS)<sub>2</sub>. B3LYP-GD3B/StuttgartRSC(Tc)/StuttgartRLC+STO-3G(Te)/6-31G\*(C,N,P,Cl)/6-31G(H) level. Figure S60. Electrostatic potential (ESP) mapping of [Tc<sup>I</sup>(NO)Cl<sub>2</sub>(PPh<sub>3</sub>)<sub>2</sub>{μ<sub>2</sub>-(2-pyS)<sub>2</sub>}] at an isosurface value of 0.004 (left: transparent mesh to highlight molecular orientation, right: untransparent mesh to highlight the values). Dark blue: corresponds to a surface potential of  $8.314 \times 10^{-2}$ , while green is 0 and red is  $-8.314 \times 10^{-2}$ . B3LYP-GD3B/StuttgartRSC(Tc)/StuttgartRLC+STO-3G(S)/6-31G\*(C,N,P,Cl)/6-31G(H) level. The position of the σ-hole *trans* to the pyridyl substituent is occupied by Cl and therefore obscured, while the position of σ-hole opposite to the chalcogen-chalcogen bond is obscured by the bulk of triphenyl phosphine. Figure S61. Electrostatic potential (ESP) mapping of [Tc<sup>I</sup>(NO)Cl<sub>2</sub>(PPh<sub>3</sub>)<sub>2</sub>{μ<sub>2</sub>-(2-pySe)<sub>2</sub>}] at an isosurface value of 0.004 (top: transparent mesh to highlight molecular orientation, bottom: untransparent mesh to highlight the values). Dark blue: corresponds to a surface potential of  $8.314 \times 10^{-2}$ , while green is 0 and red is  $-8.314 \times 10^{-2}$ . The values are normalized to those of free (2-pyS)<sub>2</sub>. B3LYP-GD3B/StuttgartRSC(Tc)/StuttgartRLC+STO-3G(Se)/6-31G\*(C,N,P,Cl)/6-31G(H) level. The position of the σ-hole *trans* to the pyridyl substituent is occupied by Cl and therefore obscured, while the position of σ-hole opposite to the chalcogen-chalcogen bond is obscured by the bulk of triphenyl phosphine. Figure S62. Electrostatic potential (ESP) mapping of [Tc<sup>I</sup>(NO)Cl<sub>2</sub>(PPh<sub>3</sub>)<sub>2</sub>{μ<sub>2</sub>-(2-pyTe)<sub>2</sub>}] at an isosurface value of 0.004 (left: transparent mesh to highlight molecular orientation, right: untransparent mesh to highlight the values). Dark blue: corresponds to a surface potential of  $8.314 \times 10^{-2}$ , while green is 0 and red is  $-8.314 \times 10^{-2}$ . The values are normalized to those of free (2-pyS)<sub>2</sub>. B3LYP-GD3B/StuttgartRSC(Tc)/StuttgartRLC+STO-3G(Te)/6-31G\*(C,N,P,Cl)/6-31G(H) level. Crystallographic information file (cif). CheckCif File. Structural data file (.xyz) of the structures for the DFT calculations.

**Author Contributions:** Conceptualization, A.A., M.R.J. and U.A.; Data curation, T.E.S., S.M.R., A.A., M.J.E. and U.A.; Formal analysis, T.E.S., S.M.R., A.A. and M.J.E.; Funding acquisition, U.A.; Investigation, T.E.S., S.M.R., A.A., M.J.E., M.R.J. and U.A.; Methodology, S.M.R., M.J.E. and M.R.J.; Project administration, U.A.; Resources, U.A.; Supervision, A.A. and U.A.; Validation, S.M.R., T.E.S., M.J.E., M.R.J. and U.A.; Visualization, M.R.J. and U.A.; Writing—original draft, U.A.; Writing—review and editing, T.E.S., S.M.R., A.A., M.J.E., M.R.J. and U.A. All authors have read and agreed to the published version of the manuscript.

**Funding:** This research was funded by the German Academic Exchange Service (DAAD), Deutsche Forschungsgemeinschaft (Core Facility BIOSUPRAMOL), and Freie Universität Berlin.

**Institutional Review Board Statement:** Not applicable.

**Informed Consent Statement:** Not applicable.

**Data Availability Statement:** The original contributions presented in this study are included in the article/Supplementary Materials. Further inquiries can be directed to the corresponding author(s).

**Acknowledgments:** We gratefully acknowledge support by the Zentraleinrichtung für Datenverarbeitung of the Freie Universität Berlin by providing computational time and the Core Facility BIOSUPRAMOL of the Freie University. We are also thankful for the hospitality of Ernesto Schulz Lang (UFSM, Santa Maria, Brazil) and his team. Our special thanks go to Felipe Dornelles, Camilla Cechin, and Rodrigo Cervo for their support.

**Conflicts of Interest:** The authors declare no conflicts of interest.

## References

1. Lippolis, V.; Santi, C.; Lenardao, E.J.; Braga, A.L. *Chalcogen Chemistry*; RSC Publishing: Cambridge, UK, 2023; ISBN 978-1-83916-422-4.
2. Lenardao, E.J.; Santi, C.; Perin, G.; Alves, D. *Organochalcogen Compounds*; Elsevier Science & Techn.: Amsterdam, The Netherlands, 2022; ISBN 9780128194508.
3. Santoro, S.; Azeredo, J.B.; Nascimento, V.; Sancineto, L.; Braga, A.L.; Santi, C. The green side of the moon: Ecofriendly aspects of organoselenium chemistry. *RSC Adv.* **2014**, *4*, 31521–31535. [[CrossRef](#)]
4. Jurinic, C.K.; Belladonna, A.L.; Schumacher, R.F.; Godoi, B. Diorganyl Dichalcogenides and Copper/Iron Salts: Versatile Cyclization System to Achieve Carbo- and Heterocycles from Alkynes. *Synthesis* **2021**, *53*, 2445–2558.

5. Wang, C.; Zhang, Y.; Sun, K.; Yu, T.; Liu, F.; Wang, X. Synthesis and Application Dichalcogenides as Radical Reagents with Photochemical Technology. *Molecules* **2023**, *28*, 1998. [CrossRef] [PubMed]
6. Mugesh, G.; du Mont, W.-W.; Sies, H. Chemistry of biologically important synthetic organoselenium compounds. *Chem. Rev.* **2001**, *101*, 2125–2180. [CrossRef]
7. Alvarez-Perez, M.; Ali, W.; Marc, M.M.; Hanzlik, J.; Dominguez-Alvarez, E. Selenides and Diselenides: A Review of Their Anticancer and Chemopreventive Activity. *Molecules* **2018**, *23*, 628. [CrossRef] [PubMed]
8. Weiss, R.; Aubert, E.; Gros Lambert, L.; Pale, P.; Mamane, V. Chalcogen Bonding with Diaryl Ditellurides: Evidence from Solid State and Solution Studies. *Chem. Eur. J.* **2022**, *25*, e202200395. [CrossRef]
9. Ivanova, A.; Arsenyan, P. Rise of diselenides: Recent advances in the synthesis of heteroarylselenides. *Coord. Chem. Rev.* **2018**, *370*, 55–68. [CrossRef]
10. Cargnelutti, R.; Schumacher, R.F.; Belladonna, A.L.; Kazmierczak, J.C. Coordination chemistry and synthetic approaches of pyridyl-selenium ligands: A decade update. *Coord. Chem. Rev.* **2021**, *426*, 213537. [CrossRef]
11. Singh, A.; Kaushik, A.; Dhau, J.S.; Kumar, R. Exploring coordination preferences and biological applications of pyridyl-based organochalcogen (Se, Te) ligands. *Coord. Chem. Rev.* **2022**, *450*, 214254. [CrossRef]
12. Matsumoto, K.; Kitayama, N.; Hirao, Y.; Kurata, H.; Kubo, T. Synthesis of a cage-shaped Nickel(II) complex of bis(4-cyclohexylamino-3-pyridyl)disulfide with  $\mu_2$ -Cl bridging. *Heterocycles* **2016**, *93*, 406–410.
13. Pal, M.K.; Karmakar, G.; Shah, A.Y.; Tyagi, A.; Bhuvanesh, N.; Dey, S. Accessing copper selenide nanostructures through a 1D coordination polymer of copper(ii) with 4,4'-dipyridyldiselenide as a molecular precursor. *New J. Chem.* **2023**, *47*, 16954–16963. [CrossRef]
14. Chaudhari, K.R.; Kunwar, A.; Bhuvanesh, N.; Dey, S. Synthesis and anti-proliferative activities of amine capped Pd and Pt macrocycles of 4,4'-dipyridylselenides. *New J. Chem.* **2020**, *44*, 7329–7337. [CrossRef]
15. Pal, M.K.; Wadawale, A.P.; Cauhan, N.; Majumdar, A.G.; Subramanian, M.; Bhuvanesh, N.; Dey, S. Anticancer potential of Pd and Pt metallo-macrocycles of phosphines and 4,4'-dipyridyldiselenide. *Polyhedron* **2022**, *211*, 115547. [CrossRef]
16. Chaudhari, K.R.; Paluru, D.K.; Wadawale, A.P.; Dey, S. Allylpalladium complexes of pyridylselenolates as precursors for palladium selenides. *Inorg. Chim. Acta* **2017**, *467*, 221–226. [CrossRef]
17. Vivekananda, K.V.; Dey, S.; Wadawale, A.; Bhuvanesh, N.; Jain, V.K. Syntheses of Pd(II)/Pt(II) complexes with non-chelating 4-pyridylselenolate ligands ranging from mononuclear to macrocyclic structures and their utility as catalysts in Suzuki C-C coupling reaction. *Dalton Trans.* **2013**, *42*, 14158–14167. [CrossRef] [PubMed]
18. Dey, S.; Vivekananda, K.V.; Bhuvanesh, N. Supramolecular Pt and Pd Complexes of 4,40-dipyridylditelluride/diselenide ligands through self-assembly. *Eur. J. Inorg. Chem.* **2018**, *2018*, 3579–3586. [CrossRef]
19. Cargnelutti, R.; Delgado, C.P.; Cervo, R.; Tirloni, B.; Burrow, R.A.; Schulz Lang, E. Synthesis and structural chemistry of Co<sup>II</sup>, Cu<sup>II</sup>, Cu<sup>I</sup> and Pd<sup>II</sup> complexes containing a flexible monoselenoether ligand. *New J. Chem.* **2018**, *42*, 17185–17189. [CrossRef]
20. Santos dos Santos, S.; Cabral, B.N.; Abram, U.; Schulz Lang, E. Bis(4-pyridyl)ditelluride as starting material for the synthesis of zwitterionic compounds and metal complexes. *J. Organomet. Chem.* **2013**, *723*, 115–121. [CrossRef]
21. For Almost 200 Disulfide Complexes See: Cambridge Crystallographic Database, Vers. 5.44. Available online: <https://www.ccdc.cam.ac.uk/> (accessed on 25 December 2024).
22. Raper, E.S. Complexes of heterocyclic thionates. Part 1. Complexes of monodentate and chelating ligands. *Coord. Chem. Rev.* **1996**, *153*, 199–255. [CrossRef]
23. Raper, E.S. Complexes of heterocyclic thionates Part 2: Complexes of bridging ligands. *Coord. Chem. Rev.* **1997**, *165*, 475–567. [CrossRef]
24. Peloquin, D.M.; Schmedake, T.A. Recent advances in hexacoordinate silicon with pyridine-containing ligands: Chemistry and emerging applications. *Coord. Chem. Rev.* **2016**, *323*, 107–119. [CrossRef]
25. Kedarnath, G.; Jain, V.K. Pyridyl and pyrimidyl chalcogen (Se and Te) compounds: A family of multi utility molecules. *Coord. Chem. Rev.* **2013**, *257*, 1409–1435. [CrossRef]
26. Jain, V.K. Pyridyl and pyrimidyl chalcogenolates of coinage metals and their utility as molecular precursors for the preparation of metal chalcogenides. *New J. Chem.* **2019**, *43*, 11034–11040. [CrossRef]
27. Kienitz, C.O.; Thöne, C.; Jones, P.G. The Coordination Chemistry of 2,2'-Dipyridyldiselenide (PySeSePy), Part 2. Complexes with Manganese, Copper and Zinc. *Z. Naturforsch.* **2000**, *B55*, 587–596. [CrossRef]
28. Kienitz, C.O.; Thöne, C.; Jones, P.G. Coordination Chemistry of 2,2'-Dipyridyl Diselenide: X-ray Crystal Structures of Py-SeSePy, [Zn(PySeSePy)Cl<sub>2</sub>], [(PySeSePy)Hg(C<sub>6</sub>F<sub>5</sub>)<sub>2</sub>], [Mo(SePy)<sub>2</sub>(CO)<sub>3</sub>], [W(SePy)<sub>2</sub>(CO)<sub>3</sub>], and [Fe(SePy)<sub>2</sub>(CO)<sub>2</sub>] (PySeSePy = C<sub>5</sub>H<sub>4</sub>NSeSeC<sub>5</sub>H<sub>4</sub>N; SePy = [C<sub>5</sub>H<sub>4</sub>N(2-Se)-N,Se]). *Inorg. Chem.* **1996**, *35*, 3990–3997. [CrossRef]
29. Cargnelutti, R.; Hagenbach, A.; Abram, U.; Burrow, R.A.; Schulz Lang, E. Synthesis and structure of Au(I), Cu(I) and Cu(II) complexes with bis(2-pyridyl)diselenide: The copper complexes and its oxidation products. *Polyhedron* **2015**, *96*, 33–37. [CrossRef]

30. de Sousa Dias, R.; Cervo, R.; dos Santos Siqueira, F.; Anraku de Campos, M.M.; Schulz Lang, E.; Tirloni, B.; Schumacher, R.F.; Cargnelutti, R. Synthesis and antimicrobial evaluation of coordination compounds containing 2,2'-bis(3-aminopyridyl) diselenide as ligand. *Appl. Organomet. Chem.* **2020**, *34*, e5750. [[CrossRef](#)]
31. Dornelles da Silva, F.; Bortolotto, T.; Tirloni, B.; de Freitas Daudt, N.; Schulz Lang, E.; Cargnelutti, R. Bis(2-pyridyl)ditellane as a precursor to Co<sup>II</sup>, Cu<sup>I</sup> and Cu<sup>II</sup> complex formation: Structural characterization and photocatalytic studies. *New. J. Chem.* **2022**, *46*, 18165–18172. [[CrossRef](#)]
32. Kedarnath, G.; Jain, V.K.; Wadawale, A.; Dey, G.K. Bis(3-methyl-2-pyridyl)ditelluride and pyridyl telluroate complexes of zinc, cadmium, mercury: Synthesis, characterization and their conversion to metal telluride nanoparticles. *Dalton Trans.* **2009**, 8378–8385. [[CrossRef](#)]
33. Chauhan, R.S.; Kedarnath, G.; Rheingold, A.L.; Munoz-Castro, A.; Arratia-Perez, R.; Jain, V.K. Reactivity of Dipyridyl Ditel-lurides with (Diphosphine)Pt<sup>0</sup> and 2-Pyridyltelluroates with (Diphosphine)PtCl<sub>2</sub> and Isolation of Different Structural Motifs of Platinum(II) Complexes. *Organometallics* **2012**, *31*, 1743–1750. [[CrossRef](#)]
34. da Silva, F.D.; Simoes, C.A.D.P.; dos Santos, S.S.; Lang, E.S. Versatility of Bis(2-pyridyl)ditellane. *Chem. Select* **2017**, *2*, 2708–2712. [[CrossRef](#)]
35. Blanchard, S.S.; Nicholson, T.; Davison, A.; Davis, W.; Jones, A.G. The synthesis, characterization and substitution reactions of the mixed ligand technetium(I) nitrosyl complex *trans-trans*-[(NO)(NCCH<sub>3</sub>)Cl<sub>2</sub>(PPh<sub>3</sub>)<sub>2</sub>Tc]. *Inorg. Chim. Acta* **1996**, *244*, 121–130. [[CrossRef](#)]
36. Nicholson, T.; Chun, E.; Mahmood, A.; Mueller, P.; Davison, A.; Jones, A.G. Synthesis, spectroscopy and structural analysis of Technetium and Rhenium nitrosyl complexes. *Commun. Inorg. Chem.* **2015**, *3*, 31–39.
37. Blanchard, S.S.; Nicholson, T.; Davison, A.; Jones, A.G. Ligand substitution reactions of [Tc(NO)Cl<sub>2</sub>(PPh<sub>3</sub>)<sub>2</sub>(NCCH<sub>3</sub>)] with  $\pi$ -acceptor ligands. *Inorg. Chim. Acta* **1997**, *254*, 225–231. [[CrossRef](#)]
38. Nicholson, T.; Hirsch-Kuchma, M.; Freiberg, E.; Davison, A.; Jones, A.G. The reaction chemistry of a technetium(I) nitrosyl complex with potentially chelating organohydrazines: The X-ray crystal structure of [TcCl<sub>2</sub>(NO)(HNNC<sub>5</sub>H<sub>4</sub>N)(PPh<sub>3</sub>)]. *Inorg. Chim. Acta* **1998**, *279*, 206–209. [[CrossRef](#)]
39. DeVries, N.; Cook, J.; Davison, A.; Nicholson, T.; Jones, A.G. Synthesis and characterization of a technetium(III) nitrosyl compound: Tc(NO)(Cl)(SC<sub>10</sub>H<sub>13</sub>)<sub>3</sub>. *Inorg. Chem.* **1990**, *29*, 1062–1064. [[CrossRef](#)]
40. Grunwald, A.C.; Scholtysik, C.; Hagenbach, A.; Abram, U. One Ligand, One Metal, Seven Oxidation States: Stable Technetium Complexes with the “Kläui Ligand”. *Inorg. Chem.* **2020**, *59*, 9396–9405. [[CrossRef](#)] [[PubMed](#)]
41. Claude, G.; Salsi, F.; Hagenbach, A.; Gembicky, M.; Drance, M.J.; Neville, M.; Chan, C.; Figueroa, J.S.; Abram, U. Structural and Redox Variations in Technetium Complexes Supported by *m*-Terphenyl Isocyanides. *Organometallics* **2020**, *39*, 2287–2294. [[CrossRef](#)]
42. Jacobsen, H.; Schmalte, H.W.; Messmer, A.; Berke, H. Remarkable low symmetry hydrogen bonding network in the structure of ReCl<sub>2</sub>(NCMe)(NO)(PMe<sub>3</sub>)<sub>2</sub>. *Inorg. Chim. Acta* **2000**, *306*, 153–159. [[CrossRef](#)]
43. Jiang, Y.; Blacque, O.; Berke, H. Probing the catalytic potential of chloro nitrosyl rhenium(i) complexes. *Dalton Trans.* **2011**, *40*, 2578–2587. [[CrossRef](#)]
44. Ackermann, J.; Hagenbach, A.; Abram, U. {Tc(NO)(Cp)(PPh<sub>3</sub>)<sup>+</sup>}—A novel technetium(I) core. *Chem. Commun.* **2016**, *52*, 10285–10288. [[CrossRef](#)] [[PubMed](#)]
45. Abram, U.; Kirmse, R.; Köhler, K.; Lorenz, B.; Kaden, L. Tc(NX)Y<sub>3</sub>(Me<sub>2</sub>PhP)<sub>2</sub> Complexes (X = O or S; Y = Cl or Br). Preparation, Characterization and EPR Studies. *Inorg. Chim. Acta* **1987**, *129*, 15–20. [[CrossRef](#)]
46. Sawallisch, T.E.; Abdulkader, A.; Nowak, D.; Hagenbach, A.; Abram, U. Nitrosyl and Thionitrosyl Complexes of Technetium and Rhenium and Their Reactions with Hydrotris(pyrazolyl)borates. *Molecules* **2024**, *29*, 3865. [[CrossRef](#)]
47. Kaden, L.; Lorenz, B.; Kirmse, R.; Stach, J.; Behm, H.; Beurskens, P.T.; Abram, U. Synthesis, characterization and x-ray molecular and crystal structure of Tc(NS)Cl<sub>3</sub>(Me<sub>2</sub>PhP)(Me<sub>2</sub>PhPO)—a first example of mixed phosphine/phosphine oxide coordination. *Inorg. Chim. Acta* **1990**, *169*, 43–48. [[CrossRef](#)]
48. Abram, U.; Schulz Lang, E.; Abram, S.; Wegmann, J.; Dilworth, J.R.; Kirmse, R.; Woolins, J.D. Technetium(V) and rhenium(V) nitrido complexes with bis(diphenyl-thiophosphoryl)amide, N(SPh<sub>2</sub>)<sub>2</sub><sup>−</sup>. *J. Chem. Soc. Dalton Trans.* **1997**, 623–630. [[CrossRef](#)]
49. Kirmse, R.; Stach, J.; Lorenz, B.; Marov, I.N. EPR on tetra-*n*-butylammonium-(tetrabromo-nitrosyl-technetate(II)). *Z. Chem.* **1984**, *24*, 36–37. [[CrossRef](#)]
50. Kirmse, R.; Stach, J.; Abram, U. EPR on tetrabutylammonium tetraiodo-nitrosyltechnetate(II), (Bu<sub>4</sub>N)[Tc(NO)I<sub>4</sub>]. *Polyhedron* **1985**, *4*, 1275–1277. [[CrossRef](#)]
51. Kirmse, R.; Stach, J.; Abram, U.; Marov, I.N. Zu Struktur, Bindung und Ligandenaustauschverhalten von Nitrosyltechnetium(II)-Verbindungen. Eine EPR-Untersuchung. *Z. Anorg. Allg. Chem.* **1984**, *518*, 210–226. [[CrossRef](#)]
52. Pickardt, J.; von Chrzanowski, L.; Steudel, R.; Borowski, M.; Beck, S. Metallkomplexe von 2,2'-Dipyridyldisulfid mit Quecksilber(II)-, Cadmium(II)- und Zink(II)-Halogeniden und mit Cadmium(II)- Trifluormethansulfonat / Metal Complexes of

- 2,2'-Dipyridyldisulfide with Mercury(II), Cadmium(II), and Zinc(II) Halides and with Cadmium(II) Trifluoromethanesulfonate. *Z. Naturforsch.* **2005**, *60*, 373–376.
53. Thöne, C.; Narro, N.; Jones, P.G. Private Communication (QUWFOE) Submitted 2010 to Cambridge Crystallographic Database, Vers. 5.44. Available online: <https://www.ccdc.cam.ac.uk> (accessed on 25 December 2024).
54. Noschang-Cabral, B.; Kirsten, L.; Hagenbach, A.; Piquini, P.C.; Patzschke, M.; Abram, U. Technetium complexes with aryselenolato and aryltellurolato ligands. *Dalton Trans.* **2017**, *46*, 9280–9286. [[CrossRef](#)]
55. Roca Jungfer, M.; Abram, U.  $[\text{Tc}(\text{OH})_2(\text{CO})_3(\text{PPh}_3)_2]^+$ : A Synthone for Tc(I) Complexes and Its Reactions with Neutral Ligands. *Inorg. Chem.* **2021**, *60*, 16734–16753. [[CrossRef](#)]
56. Bandoli, G.; Mazzi, U.; Abram, U.; Spies, H.; Münze, R. Synthesis and X-ray crystal structure of tetraethylammonium bis(1,1-dicyanoethene-2,2-diselenolato)oxotechnetate(V),  $[\text{Et}_4\text{N}][\text{TcO}(\text{Se}_2\text{C}=\text{C}(\text{CN})_2)_2]$ . *Polyhedron* **1987**, *6*, 1547–1550. [[CrossRef](#)]
57. Abram, U.; Abram, S.; Stach, J.; Dietzsch, W.; Hiller, W. Technetium Complexes with 1,1-Dicyanoethene-2,2-diselenolate,  $i\text{-mns}^{2-}$ . The Crystal Structure of  $(\text{Bu}_4\text{N})_2[\text{TcN}(i\text{-mns})_2]$ . *Z. Naturforsch.* **1991**, *B46*, 1183–1187.
58. Bhasin, K.K.; Arora, V.; Klapötke, T.M.; Crawford, M. One-Pot Synthesis of Pyridyltellurium Derivatives from a Reaction with Isopropylmagnesium Chloride and X-ray Crystal Structures of Various Pyridyl Ditellurides. *Eur. J. Inorg. Chem.* **2004**, *2004*, 4781–4788. [[CrossRef](#)]
59. Romero, J.; Duran, M.L.; Garcia-Vazquez, J.A.; Castineiras, A.; Sousa, A.; Christians, L.; Zubieta, J. Direct electrochemical synthesis and crystal structure of tris(pyridine-2-selenolato)indium(III). *Inorg. Chim. Acta* **1997**, *255*, 307–311. [[CrossRef](#)]
60. Dunne, S.J.; von Nagy-Felobuki, E.I.; Machay, M.F. An Orthorhombic Polymorph of 2,2'-Dipyridyl Diselenide. *Acta Cryst.* **1998**, *C54*, 887–889. [[CrossRef](#)]
61. Nicholson, T.L.; Mahmood, A.; Muller, P.; Davison, A.; Storm-Blanchard, S.; Jones, A.G. The synthesis and structural characterization of the technetium nitrosyl complexes  $[\text{TcCl}(\text{NO})(\text{SC}_5\text{H}_4\text{N})(\text{PPh}_3)_2]$  and  $[\text{Tc}(\text{NO})(\text{SC}_5\text{H}_4\text{N})_2(\text{PPh}_3)]$ . *Inorg. Chim. Acta* **2011**, *365*, 484–486. [[CrossRef](#)] [[PubMed](#)]
62. Harris, R.K.; Becke, E.D.; Cabral de Menezes, S.M.; Goodfellow, R.; Granger, P. NMR nomenclature. nuclear spin properties and conventions for chemical shifts (IUPAC Recommendations 2001). *Pure Appl. Chem.* **2001**, *73*, 1795–1818. [[CrossRef](#)]
63. Cargnelutti, R.; Lang, E.S.; Piquini, P.; Abram, U. Synthesis and structure of  $[\text{ReOSe}(2\text{-Se-py})_3]$ : A rhenium(V) complex with selenium(0) as a ligand. *Inorg. Chem. Commun.* **2014**, *45*, 48–50. [[CrossRef](#)]
64. Roca Jungfer, M.; Hagenbach, A.; Lang, E.S.; Abram, U. Rhenium(V) Complexes with Selenolato- and Tellurolato-Substituted Schiff Bases—Released  $\text{PPh}_3$  as a Facile Reductant. *Eur. J. Inorg. Chem.* **2019**, *47*, 4974–4984. [[CrossRef](#)]
65. Roca Jungfer, M.; Lang, E.S.; Abram, U. Reactions of Schiff Base-Substituted Diselenides and -tellurides with Ni(II), Pd(II) and Pt(II) Phosphine Complexes. *Eur. J. Inorg. Chem.* **2020**, *45*, 4303–4312. [[CrossRef](#)]
66. Ernst, M.J.; Abdulkader, A.; Hagenbach, A.; Claude, G.; Roca Jungfer, M.; Abram, U.  $[\text{Tc}(\text{NO})(\text{Cp})(\text{PPh}_3)\text{Cl}]$  and  $[\text{Tc}(\text{NO})(\text{Cp})(\text{PPh}_3)(\text{NCCCH}_3)](\text{PF}_6)$ , and Their Reactions with Pyridine and Chalcogen Donors. *Molecules* **2024**, *29*, 1114. [[CrossRef](#)]
67. Bhasin, K.K.; Singh, J. A novel and convenient synthesis towards 2-pyridylselenium compounds: X-ray crystal structure of 4,4'-dimethyl-2,2'-dipyridyl diselenide and tris(2-pyridylseleno)methane. *Polyhedron* **2002**, *658*, 71–76. [[CrossRef](#)]
68. Stoll, S.; Schweiger, A. EasySpin, a comprehensive software package for spectral simulation and analysis in EPR. *J. Magn. Res.* **2006**, *178*, 42–55. [[CrossRef](#)]
69. MATLAB, Version: 24.2.0 (R2024b); The MathWorks Inc.: Natick, MA, USA, 2024.
70. Sheldrick, G. SADABS, Vers. 2014/5; University of Göttingen: Göttingen, Germany, 2014.
71. Krause, L.; Herbst-Irmer, R.; Sheldrick, G.M.; Stalke, D. Comparison of silver and molybdenum microfocus X-ray sources for single-crystal structure determination. *J. Appl. Cryst.* **2015**, *48*, 3–10. [[CrossRef](#)] [[PubMed](#)]
72. Sheldrick, G.M. Crystal structure refinement with SHELXL. *Acta Crystallogr.* **2015**, *C71*, 3–8.
73. Dolomanov, O.V.; Bourhis, L.J.; Gildea, R.J.; Howard, J.A.; Puschmann, H. OLEX2: A complete structure solution, refinement and analysis program. *J. Appl. Crystallogr.* **2009**, *42*, 339–341. [[CrossRef](#)]
74. Macrae, C.F.; Sovago, I.; Cottrell, S.J.; Galek, P.T.A.; McCabe, P.; Pidcock, E.; Platings, M.; Shields, G.P.; Stevens, J.S.; Towler, M. Mercury 4.0: From visualization to analysis, design and prediction. *J. Appl. Cryst.* **2020**, *53*, 226–235. [[CrossRef](#)] [[PubMed](#)]
75. Frisch, M.J.; Trucks, G.W.; Schlegel, H.B.; Scuseria, G.E.; Robb, M.A.; Cheeseman, J.R.; Scalmani, G.; Barone, V.; Petersson, G.A.; Nakatsuji, H.; et al. *Gaussian 16, Revision B.01*; Gaussian, Inc.: Wallingford, CT, USA, 2016.
76. Dennington, R.; Keith, T.A.; Millam, J.M. *GaussView*, Version 6; Semichem Inc.: Shawnee Mission, KS, USA, 2016.
77. Vosko, S.H.; Wilk, L.; Nusair, M. Accurate spin-dependent electron liquid correlation energies for local spin density calculations: A critical analysis. *Can. J. Phys.* **1980**, *58*, 1200–1211. [[CrossRef](#)]
78. Becke, A.D. A new mixing of Hartree–Fock and local density functional theories. *J. Chem. Phys.* **1993**, *98*, 5648–5652. [[CrossRef](#)]
79. Lee, C.; Yang, W.; Parr, R.G. Development of the Colle-Salvetti correlation-energy formula into a functional of the electron density. *Phys. Rev. B Condens. Matter Mater. Phys.* **1988**, *37*, 785–789. [[CrossRef](#)] [[PubMed](#)]

80. Andrae, D.; Haußermann, U.; Dolg, M.; Stoll, H.; Preuß, H. Energy-adjustable initio pseudopotentials for the second and third row transition elements. *Theor. Chim. Acta* **1990**, *77*, 123–141. [[CrossRef](#)]
81. Grimme, S.; Ehrlich, S.; Goerigk, L. Effect of the damping function in dispersion corrected density functional theory. *J. Comp. Chem.* **2011**, *32*, 1456–1465. [[CrossRef](#)] [[PubMed](#)]
82. Martin, J.M.L.; Sundermann, A. Correlation consistent valence basis sets for use with the Stuttgart–Dresden–Bonn relativistic effective core potentials: The atoms Ga–Kr and In–Xe. *J. Chem. Phys.* **2001**, *114*, 3408–3420. [[CrossRef](#)]
83. Bergner, A.; Dolg, M.; Küchle, W.; Stoll, H.; Preuß, H. Ab initio energy-adjusted pseudopotentials for elements of Groups 13–17. *Mol. Phys.* **1993**, *80*, 1431–1441. [[CrossRef](#)]
84. Hehre, W.J.; Ditchfield, R.; Stewart, R.F.; Pople, J.A. Self-Consistent Molecular Orbital Methods. IV. Use of Gaussian Expansions of Slater-Type Orbitals. Extension to Second-Row Molecules. *J. Chem. Phys.* **1970**, *52*, 2769–2773. [[CrossRef](#)]
85. Pietro, W.J.; Levi, B.A.; Hehre, W.J.; Stewart, R.F. Molecular orbital theory of the properties of inorganic and organometallic compounds. 1. STO-NG basis sets for third-row main-group Elements. *Inorg. Chem.* **1980**, *19*, 2225–2229. [[CrossRef](#)]
86. Pietro, W.J.; Blurock, E.S.; Hout, R.F.; Hehre, W.J.; DeFrees, D.J.; Stewart, R.F. Molecular orbital theory of the properties of inorganic and organometallic compounds. 2. STO-NG basis sets for fourth-row main-group Elements. *Inorg. Chem.* **1981**, *20*, 3650–3654. [[CrossRef](#)]
87. Francl, M.M.; Pietro, W.J.; Hehre, W.J.; Binkley, J.S.; Gordon, M.S.; DeFrees, D.J.; Pople, J.A. Self-consistent molecular orbital methods. XXIII. A polarization-type basis set for second-row elements. *J. Chem. Phys.* **1982**, *77*, 3654–3665. [[CrossRef](#)]
88. Gordon, M.S.; Binkley, J.S.; Pople, J.A.; Pietro, W.J.; Hehre, W.J. Self-consistent molecular-orbital methods. 22. Small split-valence basis sets for second-row Elements. *J. Am. Chem. Soc.* **1982**, *104*, 2797–2803. [[CrossRef](#)]
89. Hariharan, P.C.; Pople, J.A. The influence of polarization functions on molecular orbital hydrogenation Energies. *Theor. Chim. Acta* **1973**, *28*, 213–222. [[CrossRef](#)]
90. Hehre, W.J.; Ditchfield, R.; Pople, J.A. Self-Consistent Molecular Orbital Methods. XII. Further Extensions of Gaussian-Type Basis Sets for Use in Molecular Orbital Studies of Organic Molecules. *J. Chem. Phys.* **1972**, *56*, 2257–2261. [[CrossRef](#)]
91. Ditchfield, R.; Hehre, W.J.; Pople, J.A. Self-Consistent Molecular-Orbital Methods. IX. An Extended Gaussian-Type Basis for Molecular-Orbital Studies of Organic Molecules. *J. Chem. Phys.* **1971**, *54*, 724–728. [[CrossRef](#)]
92. Ackermann, J.; Abdulkader, A.; Scholtysik, C.; Jungfer, M.R.; Hagenbach, A.; Abram, U. [Tc<sup>I</sup>(NO)X(Cp)(PPh<sub>3</sub>)] Complexes (X<sup>−</sup> = I<sup>−</sup>, I<sub>3</sub><sup>−</sup>, SCN<sup>−</sup>, CF<sub>3</sub>SO<sub>3</sub><sup>−</sup>, or CF<sub>3</sub>COO<sup>−</sup>) and Their Reactions. *Organometallics* **2019**, *38*, 4471–4478. [[CrossRef](#)]
93. Roca Jungfer, M.; Elsholz, L.; Abram, U. Technetium Hydrides Revisited: Syntheses, Structures and Reactions of [TcH<sub>3</sub>(PPh<sub>3</sub>)<sub>4</sub>] and [TcH(CO)(PPh<sub>3</sub>)<sub>2</sub>]. *Organometallic* **2021**, *40*, 3095–3112. [[CrossRef](#)]
94. Roca Jungfer, M.; Elsholz, L.; Abram, U. Technetium(I) Carbonyl Chemistry with Small Inorganic Ligands. *Inorg. Chem.* **2022**, *61*, 2980–2997. [[CrossRef](#)]
95. Ernst, M.J.; Roca Jungfer, M.; Abram, U. Reactions of Tc<sup>I</sup>(NO) and Tc<sup>V</sup>N Complexes with Alkynes and Alkynides. *Organometallics* **2022**, *41*, 2011–2021. [[CrossRef](#)]
96. Perdew, J.P. Density-functional approximation for the correlation energy of the inhomogeneous electron gas. *Phys. Rev. B* **1986**, *33*, 8822–8824. [[CrossRef](#)] [[PubMed](#)]
97. Franzke, Y.J.; Treß, R.; Pazdera, T.M.; Weigend, F. Error-consistent segmented contracted all-electron relativistic basis sets of double- and triple-zeta quality for NMR shielding constants. *Phys. Chem. Chem. Phys.* **2019**, *21*, 16658–16664. [[CrossRef](#)] [[PubMed](#)]
98. Bühl, M.; Golubnychiy, V. Density-functional computation of (99)Tc NMR chemical shifts. *Magn. Reson. Chem.* **2008**, *46*, 36–44. [[CrossRef](#)]
99. Chatterjee, S.; Holfeltz, V.E.; Hall, G.B.; Johnson, I.E.; Walter, E.D.; Lee, S.; Reinhart, B.; Lukens, W.W.; Machara, N.P.; Levitskaia, T.G. Identification and Quantification of Technetium Species in Hanford Waste Tank AN-102. *Anal. Chem.* **2020**, *92*, 13961–13970. [[CrossRef](#)] [[PubMed](#)]
100. de Andrade, T.F.C.B.; Dos Santos, H.F.; Fonseca Guerra, C.; Paschoal, D.F.S. Computational Prediction of Tc-99 NMR Chemical Shifts in Technetium Complexes with Radiopharmaceutical Applications. *J. Phys. Chem.* **2022**, *A126*, 5434–5448. [[CrossRef](#)]
101. Chatterjee, S.D.; Andersen, A.; Du, Y.; Engelhard, M.H.; Hall, G.B.; Levitskaia, T.G.; Lukens, W.W.; Shutthanandan, V.; Walter, E.D.; Washton, N.M. *Characterization of Non-Pertechnetate Species Relevant to the Hanford Tank Waste*; Tech. Report PNNL-26265; Pacific Northwest National Laboratory: Columbus, OH, USA, 2017.
102. Hall, G.B.; Andersen, A.; Washton, N.M.; Chatterjee, S.; Levitskaia, T.G. Modelling of <sup>99</sup>Tc NMR chemical shifts. *Inorg. Chem.* **2016**, *55*, 8341–8347. [[CrossRef](#)] [[PubMed](#)]
103. Luksic, S.A.; Kim, D.; Levitskaia, T.; Chatterjee, S.; Lukens, W.; Kruger, A.A. Redox and volatility of Tc(CO)<sub>3</sub><sup>+</sup> compounds in waste glass melting. *J. Nucl. Mat.* **2019**, *515*, 199–205. [[CrossRef](#)]
104. Kuznetsov, V.V.; Poineau, F.; German, K.E.; Filatova, E.A. Pivotal role of <sup>99</sup>Tc NMR spectroscopy in solid-state and molecular chemistry. *Commun. Chem.* **2024**, *7*, 259. [[CrossRef](#)]
105. Schuchardt, K.L.; Didier, B.T.; Elsethagen, T.; Sun, L.; Gurumoorthi, V.; Chase, J.; Li, J.; Windus, T.L. Basis Set Exchange: A Community Database for Computational Sciences. *J. Chem. Inf. Model.* **2007**, *47*, 1045–1052. [[CrossRef](#)] [[PubMed](#)]

106. Grimme, S. Supramolecular Binding Thermodynamics by Dispersion-Corrected Density Functional Theory. *Chem. Eur. J.* **2012**, *18*, 9955–9964. [[CrossRef](#)] [[PubMed](#)]
107. Li, Y.; Gomes, J.; Sharada, S.M.; Bell, A.T.; Head-Gordon, M. Improved Force-Field Parameters for QM/MM Simulations of the Energies of Adsorption for Molecules in Zeolites and a Free Rotor Correction to the Rigid Rotor Harmonic Oscillator Model for Adsorption Enthalpies. *J. Phys. Chem.* **2015**, *C119*, 1840–1850. [[CrossRef](#)]
108. Luchini, G.; Alegre-Requena, J.V.; Funes-Ardoiz, I.; Paton, R.S. GoodVibes: Automated Thermochemistry for Heterogeneous Computational Chemistry Data. *F1000Research* **2020**, *9*, 291. [[CrossRef](#)]
109. Lu, T.; Chen, F. Multiwfn: A multifunctional wavefunction analyzer. *J. Comput. Chem.* **2012**, *33*, 580–592. [[CrossRef](#)] [[PubMed](#)]
110. Hanwell, M.D.; Curtis, D.E.; Lonie, D.C.; Vandermeersch, T.; Zurek, E.; Hutchison, G.R. Avogadro: An advanced semantic chemical editor, visualization, and analysis platform. *J. Cheminformatics* **2012**, *4*, 1–17. [[CrossRef](#)] [[PubMed](#)]
111. Sun, H.; Li, D.; Yue, X.; Hong, R.; Yang, W.; Liu, C.; Xu, H.; Lu, J.; Dong, L.; Wang, G.; et al. A Review of Transition Metal Dichalcogenides-Based Biosensors. *Front. Bioeng. Biotechn.* **2022**, *10*, 941135. [[CrossRef](#)] [[PubMed](#)]
112. Banerjee, B.; Sharma, A.; Kaur, G.; Priya, A.; Kaur, M.; Singh, A. Latest developments on the synthesis of bioactive organotellurium scaffolds. *Phys. Sci. Rev.* **2023**, *8*, 4611–4629. [[CrossRef](#)]
113. Nobre, P.C.; Vargas, H.A.; Jacoby, C.G.; Schneider, P.H.; Casaril, A.M.; Savegnago, L.; Schumacher, R.F.; Lenardao, E.J.; Avila, D.S.; Rodrigues, L.B.L., Jr.; et al. Synthesis of enantiomerically pure glycerol derivatives containing an organovhacogen unit: In vitro and in vivo antioxidant activity. *Arab. J. Chem.* **2020**, *13*, 883–899. [[CrossRef](#)]
114. Benelli, J.L.; Poester, V.R.; Munhoz, L.S.; Melo, A.M.; Trápaga, M.R.; Stevens, D.A.; Xavier, M.O. Ebselen and diphenyl diselenide against fungal pathogens: A systematic review. *Me.d Mycol.* **2021**, *59*, 409–421. [[CrossRef](#)]
115. Nogueira, C.W.; Barbosa, N.V.; Rocha, J.B.T. Toxicology and pharmacology of synthetic organoselenium compounds: An update. *Arch. Toxicol.* **2021**, *95*, 1179–1226.

**Disclaimer/Publisher’s Note:** The statements, opinions and data contained in all publications are solely those of the individual author(s) and contributor(s) and not of MDPI and/or the editor(s). MDPI and/or the editor(s) disclaim responsibility for any injury to people or property resulting from any ideas, methods, instructions or products referred to in the content.